Evaluating remotely piloted aircraft estimates of crop height and LAI against satellite and crop model outputs

by

Omar Dzinic

A thesis
presented to the University of Waterloo
in fulfillment of the
thesis requirement for the degree of
Master of Science
in
Geography

Waterloo, Ontario, Canada, 2021

Author's Declaration

This thesis consists of material all of which I authored or co-authored see Statement of Contributions included in the thesis. This is a true copy of the thesis, including any required final revisions, as accepted by my examiners.

I understand that my thesis may be made electronically available to the public.

Statement of Contributions

I completed the majority of the data collection, analysis, and writing while Dr. Robinson provided conceptual guidance and editing.

Abstract

Crop simulation models (CSM) have been a method for decision makers to study the effects of crop management activities for predicting, planning, and improving crop growth for the past several decades. While the applicability and robustness of CSMs had been rapidly evolving, the methods of gathering input and validation data for CSMs has remained predominantly the same. However, the application of remote sensing technologies including remotely piloted aircraft systems (RPAS) and satellites for agricultural purposes has demonstrated the potential for automated rapid and high detail CSM validation data. This study evaluated the accuracy of validation data acquired using RPAS and satellite technologies when compared to CSM outputs and observed crop measurements. Imagery of an agricultural field was acquired throughout a growing season with the use of a multi-sensor RPAS and existing satellite missions. Field work was performed alongside the RPAS imagery acquisitions to collect input data for crop modelling and accuracy assessments. Using the acquired imagery, the crop height and leaf area index (LAI) values of crops in the field were estimated for multiple dates. The LAI was estimated using 1) a regression-based method and 2) a function of the fractional vegetation cover and the leaf angle distribution method. A CSM was run alongside the remote sensing to simulate crop height and LAI values. When the estimated values were compared to observed measurements, showing the RPAS-derived crop height values were significantly more accurate (RMSE=193.6 cm, RMSE=161.3 cm) than the satellite-derived crop heights values (RMSE=223.4 m, RMSE=117.1 m respectively) yet less accurate than the CSM crop heights values. The RPAS-derived LAI value accuracies (RMSE=0.42, RMSE=0.66) and satellite-derived LAI value accuracies (RMSE=0.56, RMSE=0.56) were similar but the RPAS was found to, on average, estimate LAI more accurately than the CSM. Overall, the RPAS methods showed moderate accuracy across both crop height and LAI estimations and was found to perform better than the CSM in some situations. Future work may include additional imagery acquisitions throughout a growing season to further test the accuracies of RPAS-derived estimates as well as integrating estimates directly into CSMs for validation purposes.

Acknowledgements

The first acknowledgement will have to go out to my amazing advisor, Dr. Derek Robinson, for all the work and time he committed to me during this thesis. No matter what I threw at him whether it be frustration, doubt, life complications, or schedule changes, Derek stayed level-headed and supported me through all of it. There were several times during this masters where I thought I was going to give up, but all it would take was a meeting with Derek to put me back in the right mental space and get me back on track. Derek, thank you so much for all of the academic, career, and mental support that you have provided me during this degree. I was truly lucky to have you as my advisor and the University of Waterloo is lucky to have you as a professor.

I would like to thank my committee members, Dr. Richard Kelly and Dr. Richard Petrone, for their support and guidance throughout my degree. Richard Kelly, thank you for introducing me to the amazing field that is remote sensing during my undergrad as well as answering my questions during my thesis planning. Dr. Petrone, thank you for providing me with equipment to make a significant portion of my thesis possible as well as critiquing my work.

To my fellow Geospatial Innovation Lab colleagues, Collin Branton, Veniamin Bondaruk, Bo Sun, Tanya Iljas, and Alex Smith, thank you for helping me with whatever questions I had, grabbing coffees with me, and providing support. A very special thank you to my dear friend, lab mate, and colleague, Benjamin Meinen, for always listening to my endless ranting and problems, helping me resolve whatever work issues I was dealing with, assisting me with fieldwork and data collection, and hitting me with the squash ball as infrequently as possible during matches.

Thank you to all the staff at the University of Waterloo that made completing my work possible. A huge thank you to Faye Schultz and her family (Keith and Nick) for generously providing me with a study site to perform my work on as well as answering all my questions. To all the staff in the MAD lab and the University of Waterloo IST team for providing me with necessary equipment and training as well as making the transition to remote working painless and possible. Thank you to Alan Anthony and Susie Castela for all the admin work that you have done during my time as a graduate student. Also, thank you to Kathy from the ML Tim Hortons for always cheering me up with your lovely smile and kind words.

I was incredibly lucky to also have such a supportive and caring group of friends that were always there for me. To the friends that stuck with me from the beginning of undergrad, Jack Su and Pat Filyer, thanks for helping me enjoy academia and always being there for me at the toughest times. Thanks to Mieszko Fydrych for giving me motivation to get my writing done as well helping me with the radar portion of my work. To my dear friends Brandon Van Huizen and Tasha-Leigh Gauthier, thank you for all the coffee talks that gave me the opportunity to de-stress and laugh whether they took place under the living wall or in your living room. A huge thank you to my loving and caring friends Jamieson Anderson, Caroline Kayko, and Adam Scurrah who have dealt with my inconsistent schedules and long-winded ranting but still always had time to grab a beer or McDouble with me.

Most importantly, I would like to thank my family for being with me through all of this. To my extended family split across Bosnia, Croatia, Serbia, and USA, who, due to my limited Bosnian vocabulary for technical terms, all have a different understanding of what my thesis work is based on ranging from farming to being a pilot; thank you for your constant words of encouragement and well wishes. I hope I didn't disappoint. To my dear godmother, Inci, thank you for always believing in me even when I made it quite hard to do so and always telling it to me straight. To my loving "honorary" aunt and uncle, Janet and Dr. Robert Ryan, thank you for always being there to celebrate my ups and get me through the downs as well as playing a key role in me finding a career that I love. To my wonderful and caring sister, Leila Dzinic, you were always one of my biggest supports and someone that always knew what to say no matter where you were, whether it was in the room beside me or in another continent. I look forward to more 3am coffees, PUP listening sessions, and overly zoomed-in selfies during your masters. To my partner, Kirsten Grant, words can't describe how grateful I am for everything you've done for me throughout these past few years. Not only were you my emotional rock through all the tough times but you were also someone I could always turn to for inspiration and help. Whether it was showing me how to take a soil sample or how to see the positive in a terrible situation, you were there for me and this thesis would not be submitted without you. To my loving parents, Adnan and Naila, thank you for never giving up on me no matter how bleak things looked. Thank you for always being my support system and pushing me to get through this whether it be through making me coffee every single morning to get me ready to write or learning what terms such as "baseline" or "digital surface model" mean so that you can help me work through issues. You both mean so much to me and I am incredibly fortunate to have you both in my life.

I used to think the phrase "This couldn't be done without you" was a fancy way of saying thank you, but during this thesis I have learned that it is much more literal. Therefore, thank you all so much; this couldn't have been done without you.

Dedication

I would like to dedicate this work to all of my grandparents that overcame unnecessary adversity, suffering, and hatred to allow for me to eventually accomplish what I love. Thank you and I wish you could be here to share this moment with me.

Želio bih da ovaj magistarski rad posvetim svojim djedovima i nanama koji su pretrpjeli nedaće, patnju i mržnju, kako bih ja mogao ostvariti ono što želim. Hvala Vam, i želio bih da ste ovdje sa mnom, da možemo podijeliti ovaj trenutak.

I would also like to dedicate this work to my late godfather Koray Kuzucuoğlu whose love and care for everyone and everything around him was unmatched.

Table of Contents

List of Figures

List of Tables

1.0: Evaluating remotely piloted aircraft for estimates of crop height and LAI against satellite and crop model outputs

1.1 Introduction

Crop simulation models (CSMs) formalize our understanding of how cultivated plants grow in computer code and they are often used to estimate crop growth and yield under different climate and land management activities (e.g., Jones et al., 2003; Stöckle et al., 2003). By estimating and quantifying crop growth and yield, CSMs can increase agricultural decision making capacity (e.g. Dury et al., 2012), provide a medium for knowledge transfer (e.g. Jones et al., 2003) identify new crops or management activities (e.g. Jones et al., 2003; Xiong et al., 2016), and establish critical production variables requiring attention (e.g. Bucksch et al., 2017; Gago et al., 2015). Furthermore, CSMs can provide a more cost-efficient approach to quantify the impacts of agricultural management decisions than field experiments (Nagamani & Nethaji Mariappan, 2017).

Process-based models of crop growth are particularly strong at representing how photosynthesis, competition for resources, biogeochemical cycling, and other ecophysiological processes respond to human and natural changes to site conditions, such as fertilization (e.g. Liu et al., 2011) and inundation (e.g. Pasley et al., 2020). Due to their generalized representation of the processes of plant growth, process-based models can be parameterized and calibrated for individual study areas. However, CSMs are often applied at large spatial extents using coarse resolution data (e.g. Dong et al., 2016; Moulin et al., 1998), which

produces results that are frequently inaccurate at the scale of individual farm decision makers (Dong et al., 2016).

While regional crop estimates or predictions can aid economic decision making related to food production forecasting and guide national agricultural development (e.g., H. Li et al., 2017), accurate results at the scale of the decision maker are important because it is the cumulative impacts of their individual behaviour that affect water quality (e.g., Kisekka et al., 2017) and quantity (e.g., Fortes et al., 2005; Kisekka et al., 2017; Mondal et al., 2011) and food prices (e.g., Salo et al., 2016) among other socio-environmental variables. Despite increasing global food demand (e.g., Oteng-Darko et al., 2013) and insecurity (e.g., Liu et al., 2008), increasing climate variability (e.g., Tubiello et al., 2007), and reduced sales margins (e.g., Baležentis et al., 2019), there is a need to determine the limiting variables in a crop's growth cycle across landscapes comprising heterogeneous soil, topography, and microclimate conditions. Correspondingly, there is a need to develop planning methods to mitigate the effects of those variables on crop growth and yield (Pastor-Guzman et al., 2015; Xiong et al., 2016).

Crop simulation models offer an experimental laboratory to investigate how to maximize yield and minimize environmental impact (e.g., Bendig et al., 2014; Jame & Cutforth, 1996) when they are appropriately parameterized, calibrated, and validated (Bendig et al., 2014). Data collection approaches for calibration and validation comprise destructive sampling (e.g., Jégo et al., 2011), in-field measurements (e.g., Li et al., 2015), and remote-sensing (e.g., Fan et al., 2009). While the first two approaches have traditionally provided the most accurate representation of site and situation conditions, they are limited in their spatial

coverage due to the cost and time requirements associated with manual measurement. In contrast, remote sensing data can map and quantify multiple crop and site characteristics across large spatial extents. When relationships between field measurements and remote sensing data are established, remote sensing data are frequently used to estimate crop health (e.g., NDVI, Franke & Menz, 2007; Gago et al., 2015), net primary productivity (e.g., Matsushita & Tamura, 2002; Zhao et al., 2016) and crop yield (e.g., Moulin et al., 1998). However, remote sensing data are less frequently used to calibrate and validate CSMs.

When remote sensing data have been used for CSM calibration and validation, the focus has been on quantifying crop height, leaf area index (LAI) and biomass at recurring intervals through a plant's life cycle (e.g., Dong et al., 2016; Jones et al., 2004). In rare cases, these data have been captured at sub-field resolutions (e.g., Haboudane et al., 2002), but more typically at larger regional extents (e.g., Mann & Warner, 2017). These advancements have enabled the application of crop modelling at large spatial extents (Dong et al., 2016; Moulin et al., 1998). However, novel remotely piloted aircraft systems (RPAS) operate at a scale between field-plot measurements and satellite-based imagery that: 1) align with the scale of individual decision makers; 2) has yet to be used in the calibration and validation of CSMs; and 3) must be compared to satellite derived variables to quantify the benefit of RPAS versus satellite data collection for CSM.

Despite the utility of satellite derived data for use with CSMs, the low frequency of imagery acquisition can prevent consistent topographic trend analysis (e.g., Menzies Pluer et al., 2020; Swain et al., 2007), result in cloud coverage and therefore missed data (e.g., Eberhardt et al., 2016), and the coarse spatial resolution of satellite imagery can overly

homogenize study areas (e.g., Blaschke et al., 2014). While satellites are ideal for mapping large spatial extents, more frequent or event driven collection of cloud-free, very-high resolution, imagery from RPAS can capture the spatial heterogeneity in farm fields. For example, RPAS data have been used to quantify within-field erosion (Meinen & Robinson, 2020); leaf area index (LAI; Mathews & Jensen, 2013), capture data about plant structure, including leaves, pods, and stems (Gago et al., 2015), and crop height and biomass (Bendig et al., 2015; Zheng et al., 2018). RPAS data often provide a stronger correspondence to field measurements than satellite acquired data and the cost of RPAS data acquisition is comparatively low (Hämmerle et al., 2016).

Efforts to quantify the quality of RPAS collected data relative to industry standards (e.g., 3D surface reconstruction, Meinen & Robinson, 2020; and improvements to vegetation indicies, Bendig et al., 2015) contribute to methodological advancements, and justify the use of RPAS data for scientific research. However, there remains a gap associated with the use of these data to calibrate and validate natural systems models at very high spatial resolutions, which coincide with the scale at which human decisions are made. The integration of RPAS technologies with CSMs could enhance the accuracy and performance of CSM outputs and subsequently increase farmer decision making capacity, crop yield, and overall health of the farmland.

To move beyond typical approaches used in crop monitoring (e.g., vegetation indicies) requires linking RPAS data collection efforts with CSMs to evaluate the degree to which CSMs can be calibrated and validated at the agricultural field-scale using very high resolution RPAS data. Then CSMs may be used to scale-out agricultural production and

management activities across larger spatial extents while maintaining a resolution and context relevant to the agricultural decision maker (i.e., farmers). As a step toward making the connection between RPAS data and CSMs, this thesis seeks to answer the following questions: 1) what crop simulation modelling variables can be derived from RPAS acquired data and what is their level of accuracy relative to field-based measurements; and 2) how do RPAS derived variables and CSM outputs differ in accuracy and spatial variability relative to the same variables derived through satellite imagery?

1.2 Materials and Methods

1.2.1 Study Area

The presented research is situated in Western Ontario, Canada (Figure 1), where approximately 46 percent (approximately 3,793,584 ha) of the land is been used as farmland (Ontario Ministry of Agriculture Food and Rural Affairs, 2017). The amount of farmland in Western Ontario also accounts for approximately 31%of farmland in the province of Ontario and 5.9% in Canada (Statistics Canada, 2017). Crops with the highest occupying area in Ontario were, from most area to least, soybean, grain corn (maize) and hay (Ontario Ministry of Agriculture Food and Rural Affairs, 2017).

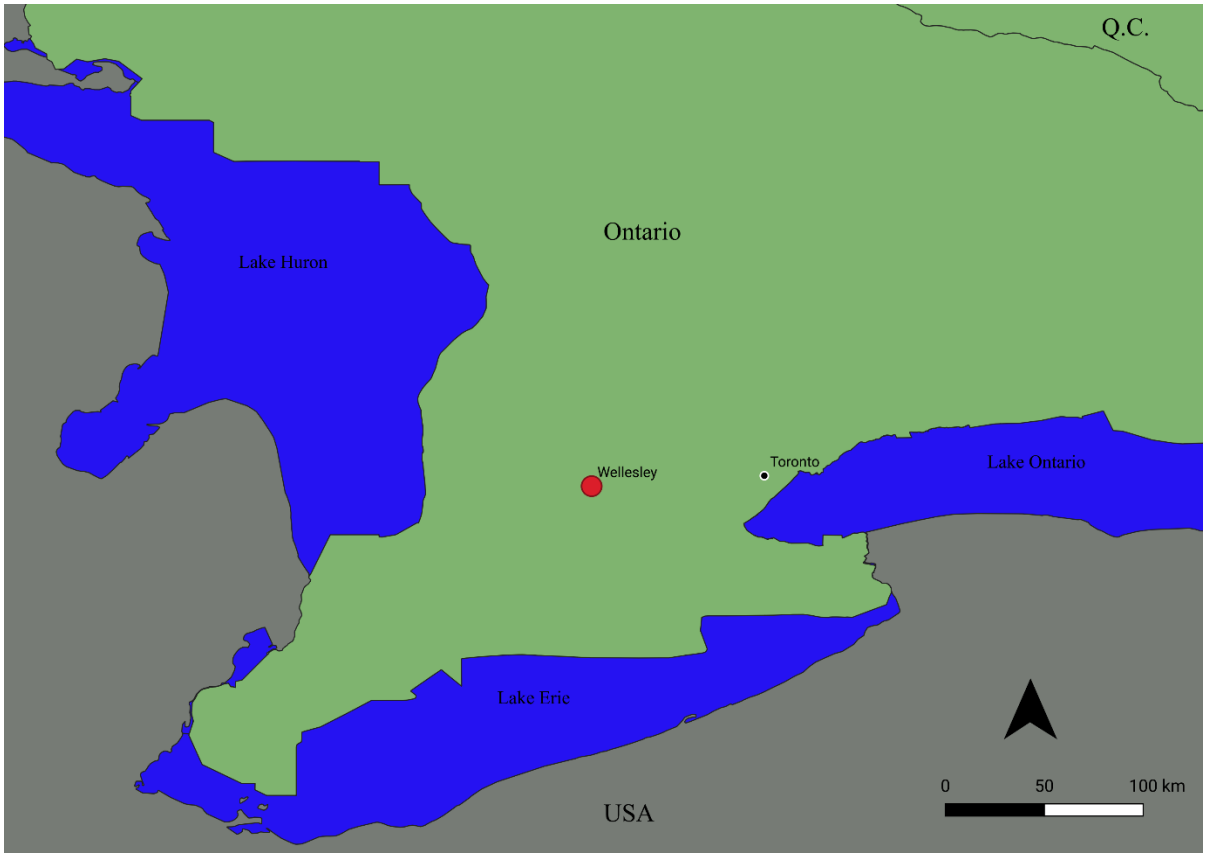

Figure 1: Study area located in the town of Wellesley in Western Ontario, Canada.

A study field was established on a farm located near Wellesley, Ontario, Canada (Figure 1). The farm field was located adjacent to the Nith River, which feeds directly into the Grand River, the largest river in southern Ontario. The farm field had an area of approximately 15.6 hectares (38.5 acres). The field consists of loam soil with approximately 50% of the loam being classified as Perth loam and approximately 50% being classified as Bennington loam (Ontario Ministry of Agriculture, Food and Rural Affairs, 2018). During the year prior to the presented study, tile drainage was installed during the winter to reduce excess water in the field. The field was tilled on May 12, 2018 and maize was planted on May 13, 2018. Fertilizers were applied three times during the growing season (May 12 N,K,P, and $(NH_4)_2S_2O_3$; May 13

N,K,P; and June 16 $(NH_4)_2SO_4$). Weather during the growing season had a mean temperature of 16.6 °C with the coldest temperature being -4.0 °C and warmest temperature being 32.5 °C. There was a total of 485.2mm of rain throughout the growing season. The maize was harvested at full maturity on November 11, 2018 after a 182-day growing season.

1.2.2 Field Measurements

Four types of in-field measurements were acquired as part of our study: soil conditions, crop height, LAI, and crop yield. Soil sampling was conducted to quantify site soil conditions, which are required to parameterize CSM site conditions. Sample locations were determined using a stratified random sampling method, whereby the study area was segmented into five slope classes with five random samples taken from each class. Slope classes were determined through several iterations of unsupervised ISO cluster classification on a slope raster of the study area generated from the Southwestern Ontario Orthoimagery Project 2015 digital surface model (DSM) (Ontario Ministry of Natural Resources and Forestry, 2015). At each sample location, a soil core was extracted using a manual 2 cm inner diameter tubular soil sampler and the top 15 cm of the extracted core was taken for analysis. The five samples taken from the same slope class were aggregated to create a single representative sample of the soil characteristics throughout the class and were placed in a cooler immediately. The five aggregated soil samples were sent to the University of Guelph's Agriculture & Food Laboratory for soil analysis (Appendix A: Soil Analyses Performed). In addition to the laboratory analysis, soil moisture was measured in the field using a Delta-T WET-2 soil moisture sensor 10 times at every slope class to be compared to the soil moisture measurements performed in the lab.

While soil samples provided parametrization of site conditions in the CSM, field measurements of crop height and LAI over the growing season were taken and used as validation data against RPAS and satellite imagery-generated crop height and LAI values. Crop height measurements were collected manually using a measuring tape. Plants were measured within a 5 m radius of ground control points (GCPs), which were measured and observed for locating and orthorectifying RPAS imagery on June 14, 2018 (see 1.2.3). At each GCP location, five of the nearest surrounding plants were measured from the ground to the highest drooped leaf to ensure that the height point would be visible in imagery captured at a nadir orientation. If the area around the GCP was unvegetated then no measurements were made in proximity to that GCP.

Leaf area index (LAI) measurements were collected using a LI-COR LAI-2200C Plant Canopy Analyzer (LI-COR Biosciences). LAI measurements were performed in two five metre transects near each GCP. Each transect started with one above-canopy light measurement followed by five below-canopy light measurements to ensure an accurate calibration. Following calibration of the Plant Canopy Analyzer, five measurements were taken at two metre intervals (for each transect) to ensure independence from previous measurements. The LAI measurements were performed during blue sky conditions between the hours of 12PM and 2PM to minimize the variation in incident solar radiation. To mitigate the effect of the individual recording the measurement on the amount of light reaching the sensor, a 270 degree cap was placed on the instrument's sensor to block out the user's body from the readings (LI-COR Inc., 2015). A total of 153 LAI measurements were recorded, but 15 were removed from

further analyses due to incorrect measurements of LAI caused by either GPS error or cloud presence. Recorded LAI values ranged from 0.29 to 4.24 with a median of 2.49.

In addition to soil, crop height, and LAI data, crop yield data were collected by a John Deere 9770 STS combine that was RTK-GPS enabled and collected point located yield values at 1.5 m intervals. Yield values were recorded in bushels per acre and stored as a Shapefile dataset comprising 65,864 points within the study field. The total wet and dry yield mass was also measured post-harvest using an industrial-sized scale to ensure the values recorded by the combine were accurate. The measured values were 208.01 metric tonnes of wet yield with a moisture percentage of 21.1% and 190.31 metric tonnes of dry yield with a moisture percentage of 15.5%.

1.2.3 RPAS Data Acquisition and Measurements

RPAS imagery was acquired through five field campaigns over the 2018 growing season (May 30; June 8, 15; July 14; and September 19). Imagery were collected using a Da-Jiang Innovations (DJI) Inspire 1 multi-rotor quadcopter () carrying two digital camera payloads. The first payload (DJI Zenmuse X3) was fully integrated in the RPAS and captured visible spectrum imagery with a 12.4 megapixel camera. A second camera, the multi-sensor Parrot Sequoia (Parrot SA), was mounted to the Inspire 1 using a 3D printed custom mount that held the camera and an incident solar radiation sensor. The Parrot Sequoia includes five sensors, a 16-megapixel RGB camera and four 1.2 megapixel single-band cameras (Red (640-680 nm), Green (530-570 nm), Red-Edge (730-740 nm), and Near-Infrared (770-810 nm)). To maximize the visibility of maize leaves in the imagery, nadir camera orientations were used. The DJI Zenmuse X3 camera operates on a gimbal that was set to and maintained a nadir orientation.

However, the Parrot Sequoia was mounted in a fixed position to approximate nadir image acquisition, which resulted in an average image angle of 8º with a standard deviation of 4.82º.

Figure 2: DJI Inspire 1 multi-rotor quadcopter with the DJI Inspire controller and batteries.

Parallel axis flight plans were flown using the Pix4Dcapture software (Pix4D Inc.) and operated on the DJI Inspire 1 Remote Controller along with a Nvidia Shield Tablet K1. Flight plans were generated to ensure comprehensive coverage of the study area; multiple overlapping imagery, which differed for each payload due to differences in field of view; and limit the number of turns performed by the RPAS to maximize flight time. Flight altitude was initialized to 90 metres above ground level at the take-off and landing site, which provided an

average ground sampling distance of three centimetres for the RGB imagery and 10 centimetres for the multispectral imagery. The RPAS was also set to fly at a medium speed setting of 6.9 m/s (25 km/hr) to ensure that the sensors have appropriate time to capture images while maintaining consistent and stable flight.

Table 1: Camera field of view and imagery overlap percentages**.**

Camera	Field of View (degrees)	Imagery Frontal Overlap (%)	Imagery Side Overlap (%)
DJI Zenmuse X3	94	85	76.5
Parrot Sequoia Multispectral	73.7	80	67.5
Parrot Sequoia RGB	73.5	79.8	67.3

Prior to each flight, 23 GCPs were placed throughout the study field to facilitate accurate georeferencing of RPAS imagery. A structure-from-motion multi-view stereo (SfM-MVS) image-processing workflow was conducted in Pix4D to derive orthomosaics of the study field. The GCPs were made from wood and were painted with a fluorescent orange paint to increase their visibility in acquired imagery (Appendix B). GCPs were distributed throughout the field with similar spacing between each, as well as being placed in locations that were easily identifiable in the acquired imagery. The location of each GCP was measured using an SmartNet RTK-enabled Leica Global Navigation Satellite System, which ensured an average accuracy of one centimetre for recorded position measurements and an average accuracy of two centimetres for elevation measurements. The use of 21 GCPs in a similar distribution throughout the field was found to result in a vertical accuracy of about 2.8 cm and horizontal

accuracy of about 1.9 cm when using the SmartNet RTK-enabled Leica Global Navigation Satellite System (Meinen & Robinson, 2020).

Imagery acquired by the RPAS was captured continuously at set distance intervals during each flight. The distance intervals varied slightly throughout the flights due to small refinements in the acquisition methodology and varying sensor GPS signal strengths. Distance intervals were every 16 m on May 30 and June 8, 25 m on June 15, 23 m on July 14, and 26 m on September 26. Before the imagery was processed, the image collection was filtered to remove those acquired at incorrect viewing angles, received overexposure, or were acquired during take-off or landing (approximately 250 images per field visit).

Images were processed using the Pix4D photogrammetry software on a workstation comprising an Intel Xeon CPU E5-1620 Quad-Core CPU, 64GB of DDR3 RAM, and a Nvidia Quadro K4200 GPU. Before each process was executed, images were georeferenced using manually recorded GCP locations in Pix4D to minimize distortion in the resulting datasets. RGB and multispectral imagery were then used with Pix4d to generate a densified point-cloud and orthomosaic for each acquisition. Point cloud densification process was run at a half image scale with a point density of 5.36 points/m^3. An orthomosaic was generated for both the RGB imagery (pixel resolution of 3.87 cm) and multispectral imagery (pixel resolution of 9.54 cm) and consisted of the same number of imagery bands as the input datasets. A multispectral orthomosaic was not generated for the May 30th acquisition due to the multispectral sensor not being mounted to the RPAS at that time. The four multispectral bands were combined into a multi-band raster and clipped to the study area for simplicity in further processing. The multi-band rasters were then used to generate several commonly used vegetation indicies, which

included: the Difference Vegetation Index (DVI), Soil Adjusted Vegetation Index (SAVI), and Normalized Difference Vegetation Index (NDVI). These vegetation indices were generated using the Raster Calculator tool in QGIS (Table 2). For the SAVI calculation, the L parameter represented a soil brightness correction factor to adjust the final value to the amount of vegetation cover in the field. The L parameter ranges from 0 to 1, with 0 indicating full vegetation cover and 1 indicating no vegetation cover. An L value of 0.5 was assigned to match similar studies using RPAS (Candiago et al., 2015) and satellite (Galletti & Myint, 2014) platforms. The final number of products generated from the RPAS imagery were five GeoTIFF rasters per acquisition date, excluding May 30th, totalling 21 GeoTIFF rasters.

The calculation of crop heights from RPAS data acquisition involved the generation of 3D point clouds and subsequent digital terrain and surface models using SfM-MVS and Pix4D. Using the May 30th RPAS imagery, acquired prior to the presence of vegetation, a digital terrain model was generated. Then digital surface models were created using imagery acquired at each subsequent flight campaign over the growing season to capture crop height and non-vegetated surfaces (e.g., roads, buildings). Non-vegetated surfaces were used to co-register all 3D models (Digital Terrain Model (DTM) and DSMs) in CloudCompare and converted to GeoTiff rasters with a 4 cm resolution. Then simple change detection methods were used to quantify crop height by subtracting the DTM from the DSMs. Crop heights with a 5 m radius of each GCP were averaged for comparison with field measurements.

LAI values of maize plants were calculated using two approaches. The first approach involved regressing in-field LAI measurements against 13 inputs derived from RPAS acquired imagery (Table 2). The Exploratory Regression tool in ArcGIS (Environmental Systems

Research Institute) was used to evaluate all possible combinations of independent variables. While the tool conducts a number of assessments of regression performance, it evaluates the performance of each regression model based on R^2 and number of explanatory variables. From among the top ten models identified by ArGIS, a single model was selected based on a combination of having a high R^2 value, low variance inflation factor (VIF), and more statistically significant coefficients ($p<0.01$). This model was then applied across the study field to derive LAI values using the Raster Calculator from QGIS (Quantum GIS).

The second approach calculated LAI as a function of the fractional vegetation cover and the leaf angle distribution (Choudhury et al. 1994). Fractional vegetation cover was calculated as follows:

$$f = 1 - \frac{NDVI_{nax} - NDVI}{NDVI_{max} - NDVI_{min}}^{1/\zeta}$$

where ζ represents the canopy leaf angle distribution value, which is used to define the orientation of the leaves on a crop and *f* represents the fractional vegetation cover value (Thorp et al., 2012; Unigarro M. et al., 2017).

Having obtained *f*, LAI at each location was calculated using the following equation:

$$LAI = \frac{\ln(1-f)}{-\beta}$$

where β is the second function of leaf angle distribution with a range of 0.42 to 0.91 (Thorp et al., 2012). The value of β (0.68) was obtained through a calibration procedure that adjusted ζ

to minimize the error between field measurements and calculated (Choudhury et al., 1994) LAI values. The resulting ζ value was 0.76. Similar to crop height measurements, LAI calculations were averaged within a 5 m radius of each GCP for comparison with field measurements.

Table 2: Input metrics for creating LAI regressions equation using RPAS imagery.

Regression Input	Metric Calculation
Difference Vegetation Index (DVI)	$NIR - RED$
Soil Adjusted Vegetation Index (SAVI)	$\frac{NIR - RED}{(NIR + RED + L)(1 + L)}$
Normalized Difference Vegetation Index (NDVI)	$\frac{NIR - RED}{NIR + RED}$
Aspect	Derived from slope data
Height	Derived through stereoscopic photogrammetry
DJI Imagery Band Rasters (Red band, Green band, Blue Band)	-
Parrot Sequoia Imagery Band Rasters (Red band, Green band, Blue band, NIR band, Red-Edge Band)	-

1.2.4 Satellite Data Acquisition and Measurements

To assess the usability of RPAS data for calibrating and validating crop growth models and the performance of those models relative to satellite-acquired remote sensing data, we acquired Sentinel-2A, Sentinel-2B, and Sentinel-1 satellite data from the European Space Agency's Copernicus Open Access Hub (Tzouvaras et al., 2020). The Sentinel-2 satellites are equipped

with multi-spectral sensors that capture visible, near infrared and short-wave infrared wavelengths at pixel resolutions from 10 m to 60 m (Drusch et al., 2012). The Sentinel platforms provide the finest spatial resolution imagery that are freely available and capture similar spectral wavelengths to those used by the RPAS in this study. Furthermore, the temporal resolution of the Sentinel-2 platforms of five days facilitates matching acquisition dates between Satellite and RPAS flights within a margin of three days. In total, 10 Sentinel-2 images matched our field campaign dates; however, two images contained cloud cover and were excluded. The Sentinel-2 imagery was used to calculate LAI and vegetation indicies. The retrieved data archives were extracted as 14 JPEG2000 Sentinel-2 bands per dataset. Of the 14 bands, the following four were used: blue (490 nm), green (560 nm), red (665 nm), and near-infrared (842 nm). These bands were combined into the same vegetation indices derived by RPAS collected imagery (DVI, SAVI, and NDVI). For the calculation of SAVI values, the same L values were used as the RPAS SAVI calculations. These four products (i.e., LAI, DVI, SAVI, and NDVI) were generated for each Sentinel-2 image, excluding May 30th, totalling 16 images.

While the Sentinel-2 imagery was appropriate for deriving CSM parameters from optical imagery (e.g., LAI), the spatial resolution and percent-of-image overlap was not suitable for deriving measurements of crop height using SfM-MVS. To calculate crop heights, radar data were acquired through the European Space Agency's Sentinel-1 mission. The Sentinel-1 mission covered the extent of our study area, had a similar temporal resolution to other datasets used, higher pixel resolution relative to other available sensor platforms and had dates of data acquisition available that aligned with RPAS data acquisition dates. The Sentinel-

1 also had a revisit time (12 days) and spatial resolution (approximately 13m) that were similar to the Sentinel-2 data.

The Sentinel-1 imagery were used to derive estimates of crop height using interferometric methods. Differences in waves or phases between image pairs can be measured to create a product called an interferogram. Interferograms map these differences for discrete locations, which can be used to generate DTM and DSMs of an area (Yu et al., 2010). Differences in the Sentinel-1 phase data, represented in generated interferograms, represent the relative difference in topography and subsequently crop heights at later collection dates. Sentinel-1 data, the Interferometric Wide Swath Single Look Complex (IW SLC), are collected using synthetic aperture radar at 250 km wide swaths through a series of c-band microwave bursts. A requirement of interferometry is that pairs of images are collected that cover the same sensing areas within a similar time period and have a low baseline value between each other. The baseline value is an indication of the alignment of the image pair, which is a critical factor affecting the interferograms accuracy. It is recommended that Sentinel-1 paired imagery obtain a baseline value under five km, also known as the critical baseline (Chen et al., 2020), since higher values reduce the coherence among image pairs in the interferometric process. Ten IW SLC products were collected for the crop height calculations with acquisitions on April 28 and May 10, 2018 paired to generate a bare ground DTM and the following acquisitions paired to coincide with RPAS data acquisition dates: May 22 and June 3, RPAS May 30; June 15 and 27, RPAS June 8; July 9 and 21, RPAS July 14; and September 7 and 19, 2018, with RPAS September 19.

Deriving crop heights from the remotely sensed Sentinel-1 data was done by creating DSMs using an interferometric approach with the ESA's Sentinel Application Platform (SNAP) program (Tzouvaras et al., 2020). The SNAP process involved three steps: interferogram formation, interferogram filtering, and interferogram to DSM conversion. The interferogram formation and interferogram filtering steps were automated using SNAP's Graph Builder, which allows the user to create an automated workflow by combining multiple tools and outputs. Interferograms were formed for each IW SLC image pair, using a custom SNAP graph, by first extracting data covering the study site. Then, the extracted data were co-registered by updating orbit data and backgeocoding to ensure accurate alignment (Lazecký et al., 2018). Lastly, the interferogram tool was used to generate interferogram and coherence rasters. The coherence raster quantifies the correlation between the paired images and provides a measure of accuracy for corresponding pixels in the interferogram (Yu et al., 2010). The interferogram formation process was run for each IW SLC pair resulting in six interferograms.

The second step in the SNAP process involved filtering each interferogram to remove seamlines and reduce noise that was incorrectly picked up as phase data. Seamlines are errors that generate data gaps when IW SLC images are stitched together. Seamline errors were corrected by using overlapping burst data between the stitched images to fill the gaps, producing a continuous product (S-1 TOPS Deburst SNAP tool; Tzouvaras et al., 2020). Following the seamline correction, noise caused by thermal interference as well as temporal changes in topography between image acquisitions were filtered out (Goldstein Phase Filtering tool; Goldstein & Werner, 1998).

The third and final step in the SNAP process involves converting the interferogram to a DSM using a process known as phase unwrapping (Chen & Zebker, 2002). Phase unwrapping converts the phase values in an interferogram to relative difference values by comparing a target cell with neighbouring pixels in the interferogram raster (Chen & Zebker, 2002). This comparison allows for differences to be calculated between the phase values, which can be used to generate metrics such as elevation values due to the phase values having coordinate information tied to them. Phase unwrapping was performed using the Statistical-Cost, Network-Flow Algorithm for Phase Unwrapping (SNAPHU; Appendix D: SNAPHU Methodology), which is compatible with several SNAP tools and yields a higher accuracy compared to alternative methods (Chen & Zebker, 2002). The unwrapped interferograms were then imported into SNAP and converted to elevation rasters using the Phase to Elevation tool (S1TBX - ESA Sentinel-1 Toolbox v8.0.0) and geocoded for UTM Zone 17 using the Terrain Correction tool (S1TBX - ESA Sentinel-1 Toolbox v8.0.0) to ensure spatial and height-unit (metres) consistency with the other spatial datasets. The outcome of the SNAP process included six DSM rasters with respective coherence bands at a 13 m spatial resolution. All output rasters were coregistered and crop height data were derived by subtracting the May 1St radar-generated DTM from each of the five interferometry-generated DSMs using the QGIS Raster Calculator.

LAI was calculated using Sentinel-2 imagery using the same regression approach as was conducted with the RPAS data. However, in this case the following variables were used: crop height, aspect of the crops, and NDVI. Similarly, the second approach to calculating LAI,

as a function of the fractional vegetation cover and leaf angle distribution (Choudhury et al. 1994), was also applied in the same manner as conducted for RPAS data.

1.2.5 Leaf Area Index Accuracy Assessment

LAI in-situ measurements from September 19, 2018 were used as validation measurements for an accuracy assessment of the generated LAI values using the regression-based approach and Choudhury et al. (1994) approach for both RPAS and Satellite data. Correspondence between RPAS and Satellite platforms was determined by computing the differences between the observed and estimated LAI values. In total, 138 LAI measurements were available for the comparison but were differentially aggregated to accommodate the different spatial resolutions of the RPAS and Satellite data. All 138 points were used in comparison with RPAS estimates. However, to coincide with the 10 m resolution of the Sentinel data, the 138 points were aggregated up to 22 measurements of average LAI (Figure 3).

Figure 3: (Left) Map of observed LAI points used in RPAS-derived LAI accuracy assessment, and (Right) Map of aggregated observed LAI points used in Sentinel-derived LAI accuracy assessment.

To retrieve calculated LAI values from the generated rasters, the Point Sampling Tool Plugin in QGIS was used. For each raster, the relevant observed measurement feature class was used as an input for where to extract the values and a comparison table was generated. The tables contained a column of feature IDs, observed LAI measurements, and calculated LAI values for each measured location. Accuracy was determined by calculating the absolute difference between observed and calculated LAI values for each location.

To test the effect of the aggregation of field measurements for validating Sentinel estimates, a similar process was done with a 10 m radius averaging of the RPAS LAI values. Averages were calculated by buffering the centroids of Sentinel raster pixels and using Zonal Statistics to calculate mean LAI values from the RPAS LAI rasters. These mean LAI values were then compared to the same aggregated measurement points as done for the Sentinel accuracy assessment.

1.2.6 Meteorological Data

Meteorologic data were acquired from Environment and Climate Change Canada (Environment and Climate Change Canada, 2018) for 2018 as CSM input. Data were recorded approximately 30 km from the field site at Roseville, Ontario and comprised daily high and low temperature values, total precipitation, and dew point temperature. In addition to these data, daily solar radiation data were acquired from NASA (Sparks, 2018).

1.2.7 Crop Simulation Modelling

Crop simulations were conducted using the DSSAT-CERES-Maize simulation model (Liu et al., 2011) that consisted of the CERES-Maize model incorporated into the Decision Support for Agrotechnology Transfer (DSSAT) modelling software suite (Jones et al., 2003). DSSAT-CERES-Maize is a process-oriented model that combines climate, soil characteristics, nutrient and water availability, and root development with agricultural land management activities such as fertilizer and irrigation applications, planting, and harvesting to simulate the growth of maize crops (Jones et al., 2003). The model has limited input requirements, which has made the model very accessible for agricultural scientists and facilitated its application to over 29

different crop types around the world, including maize growth studies in Southern Ontario (Dong et al., 2016; Liu et al., 2011).

Parametrization of the model was done using a crop management data generation tool (Xbuild) that is a part of the DSSAT suite. Xbuild consists of configuration windows that accept input data for a number of crop management factors including soil analysis, initial field conditions, cultivars used, planting/harvesting methods and dates, fertilizer applications, and chemical applications. Initialization of site conditions in DSSAT utilized results from field measurements (e.g., plant density) and soil analysis. Weather conditions were input using daily weather data for Roseville, Ontario acquired from Environment Canada, converted to a format compatible with DSSAT using the Weatherman tool (Pickering et al., 1994). Weatherman is a part of the DSSAT suite and is used for structuring weather data into a standard format for DSSAT simulations as well as checking for data errors that would normally cause issues in the simulation (Nyang'Au et al., 2014; Pickering et al., 1994). Converted weather data contained values for minimum and maximum daily temperature, precipitation, solar radiation, and dew point.

Land management was initialized by first specifying the cultivar of maize (P9621AMXT, Pioneer 9621) planted in the study field. In absence of this cultivar being available in DSSAT, PIO 3790 (Pioneer 3790) was used as it was developed by the same company and used in previous maize modelling in Ontario with DSSAT-CERES-Maize (Liu et al., 2011). Planting date (May 13, 2018), planting method, planting distribution metrics, and harvest date (November 11, 2018) were parameterized with values obtained directly from the farmer and in-field measurements. One chemical and five fertilizer applications were

conducted throughout the growing season, which included herbicide, ammonium fertilizer, and potash as reported by the farmer.

The model was configured to simulate crop growth using a daily timestep over the growing season (May 13th to November 11th, 2018). Five simulations were conducted to test the effects of different soil conditions (e.g., texture and nutrients) by parameterizing the soil conditions with results from each of the five soil sample analysis data. All other parameters were constant across all five simulations. Simulation outputs were reported in their smallest units for comparison, which for all available phenology metrics including canopy height and LAI were at a field-scale while crop yield was reported per-hectare.

1.2.8 Statistical Tests

Statistical tests were performed on comparisons of crop height and LAI values from the RPAS and satellite acquisitions to determine if statistically significant differences existed. The Shapiro-Wilk test for normality (Shapiro & Wilk, 1965) determined that crop height and LAI values followed a normal, parametric distribution. A Brown-Forsythe test (Brown & Forsythe, 1974) was then used to assess variance among compared distributions, which found equal variance for one of the comparisons and unequal variance for the remaining comparisons. To determine if there was significant difference for the comparisons, a Two-Sample Independent t-test was performed on the one comparison with equal variances and the Welch's t-test (Welch, 1947) was performed on the remaining comparisons with unequal variances.

1.3 Results

1.3.1 Crop Height

Evaluation of RPAS crop height estimates to field observations comprised 18 comparisons using data collected on June 15th and 11 comparisons using data collected on September 19, 2018 (Section 1.2.3). Our June 15th field-based measurements had an average crop height of 43.3 cm across all 18 measured locations, with a standard deviation of 11.8 cm, and minimum and maximum values of 12.0 cm and 69.0 cm, respectively. The RPAS data-derived crop height values were greater than the observed height values with an average height of 168.1 cm across the 11 sample locations. The standard deviation, minimum, and maximum RPAS data-derived crop height values were 155.6, -86.3, and 418.5 cm, respectively. The minimum value of –86.3 cm indicated that there was an error in the SfM-MVS calculation in that location. The June 15th RPAS-derived DSM minus the May DTM (Figure 4), produced an average crop height of 209 cm across the entire study area. When the measured points were compared to the RPAS data-derived values, a mean residual of 155.6 cm, minimum residual of 0.44 cm, maximum residual of 360.3 cm, and standard deviation of 120.3 cm was calculated for June. RMSE of the RPAS data-derived values was 193.6 cm. The largest residual value (360.3 cm) was located in the southwestern section of the study area while the smallest (0.44 cm) was found in the eastern section.

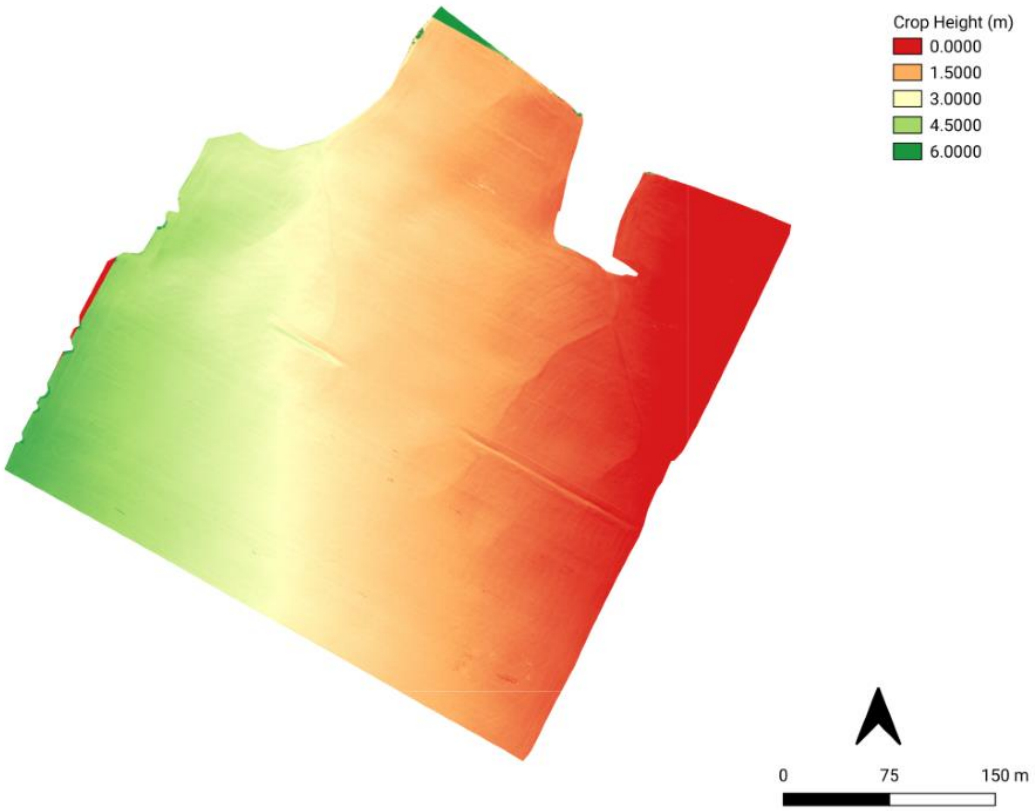

Figure 4: Map of crop heights derived from the June 15th RPAS imagery.

September 19th field observations produced an average crop height of 197.3 cm among the 11 measured locations with a standard deviation of 26.6 cm, and minimum and maximum crop heights of 134.6 cm and 246.38 cm, respectively. Again, RPAS data-derived crop height values were substantially greater than observed height values, whereby the average across the 11 sample locations was 303.7 cm. The standard deviation, minimum, and maximum RPAS data-derived crop heights were 132.8 cm, 82.0 cm, and 581.1 cm, respectively. September 19th RPAS derived DSM minus our May DTM (Figure 5), produced an average crop height value across the entire study area of 367 cm. When the observed measurement points were compared to the RPAS data-derived values (Figure 6), a mean residual of 129.0 cm, minimum residual

of 6.4 cm, maximum residual of 344.3 cm, and standard deviation of 101.8 cm was calculated for September. RMSE of the RPAS data-derived values was 161.3 cm. The largest residual value (344.3 cm) was located in the western section of the study area while the smallest (6.4 cm) was found in the southeastern section. When the residual errors of the June 15th and September 19th RPAS crop height values were compared (Figure 7), it was found that the difference between them was statistically significant (p=0.025).

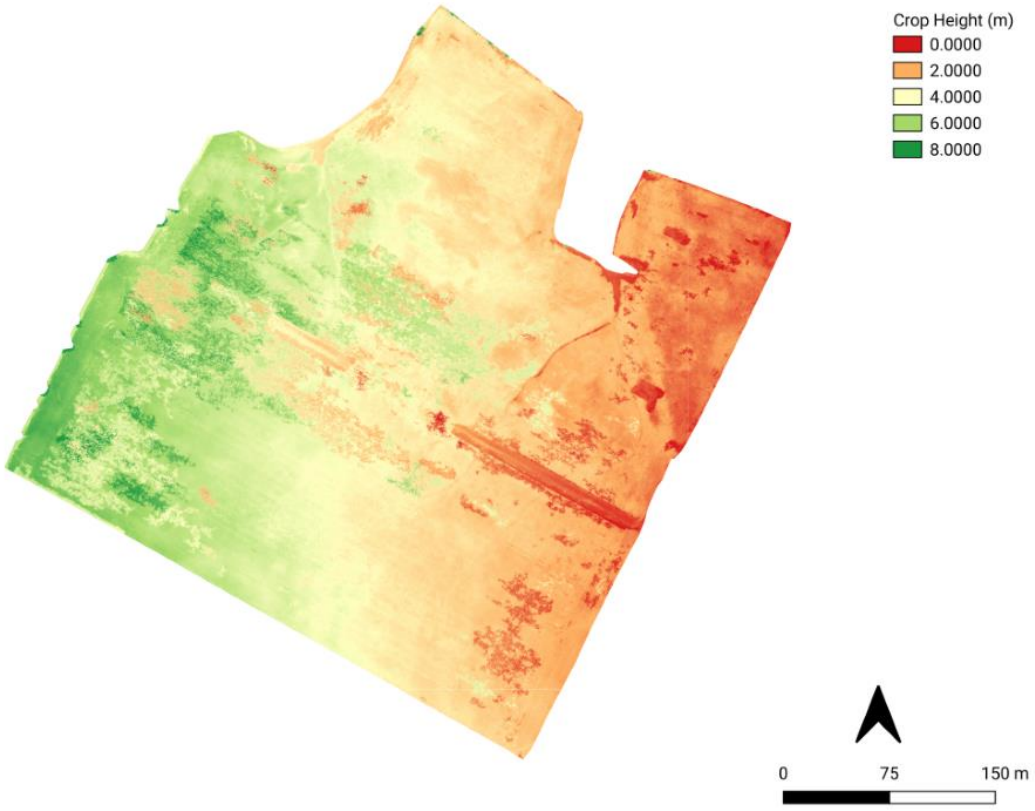

Figure 5: Map of crop heights derived from the September 19th RPAS imagery.

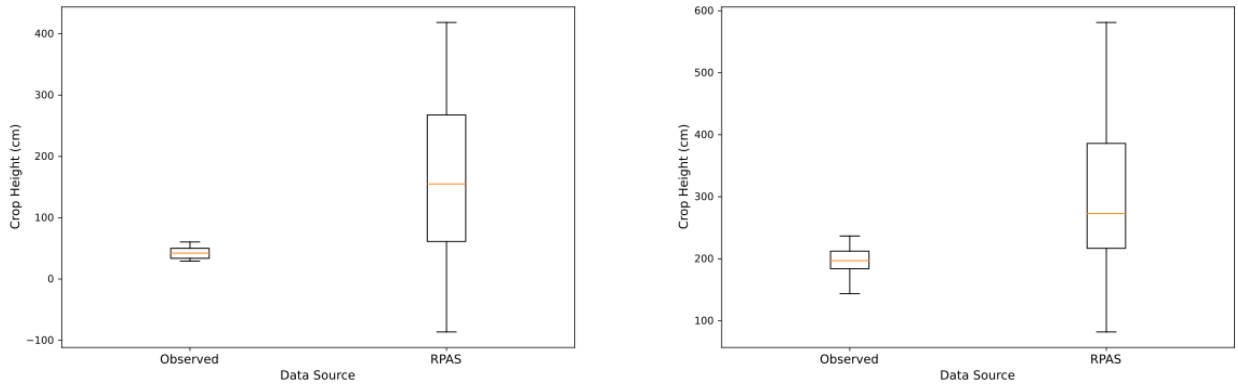

Figure 6: (Left) Distribution of crop height values between the observed data and RPAS-derived data for the June 15, 2018 data collection (Right) Distribution of crop height values between the observed data and RPAS-derived data for the September 19, 2018 data collection.

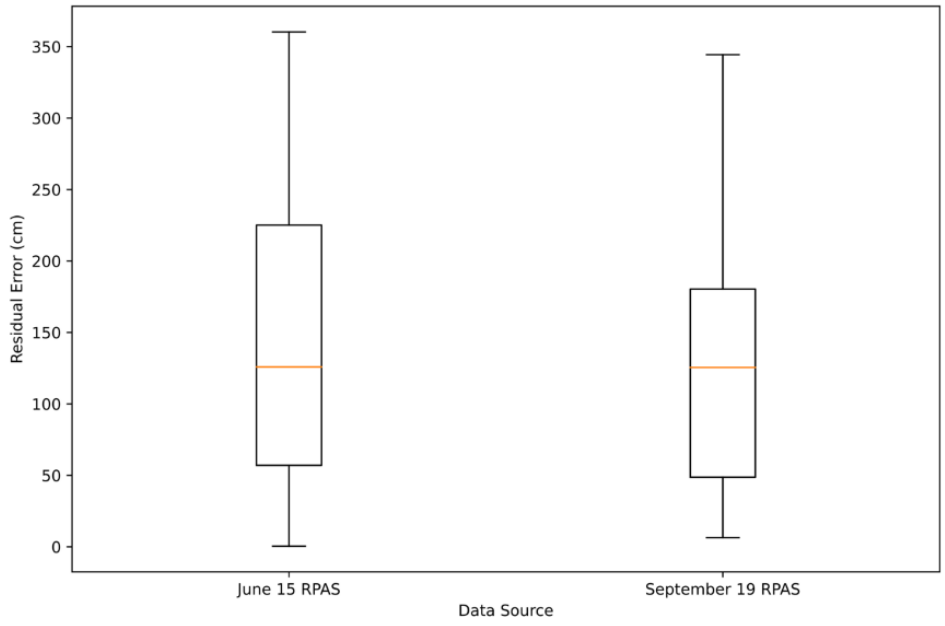

Figure 7: Distribution of crop height residual errors from the accuracy assessments performed on the RPAS-derived crop height values for June 15, 2018 and September 19, 2018.

While crop height values acquired from RPAS were less accurate than expected, crop height values calculated using the Sentinel imagery incurred much larger error and varied greatly throughout the study area. Crop height values were heavily skewed to the left, which consisted of a high frequency of negative values that greatly affected mean crop height calculations. Crop heights derived from the June 15th Sentinel DSM minus the May DTM (Figure 8), yielded a mean value of –133.5 m (Figure 9). When Sentinel-derived crop height values were compared to the 11 measured locations (Figure 10), the mean residual was 185.4 m with a minimum residual of 16.8 m, maximum residual of 522.1 m, and standard deviation of 128.8 m. The RMSE of Sentinel data-derived values was 223.4 m. The location of the smallest residual (16.8 m) was on the eastern side of the study area, and the location with the largest residual (52.2. m) was in the northeast corner.

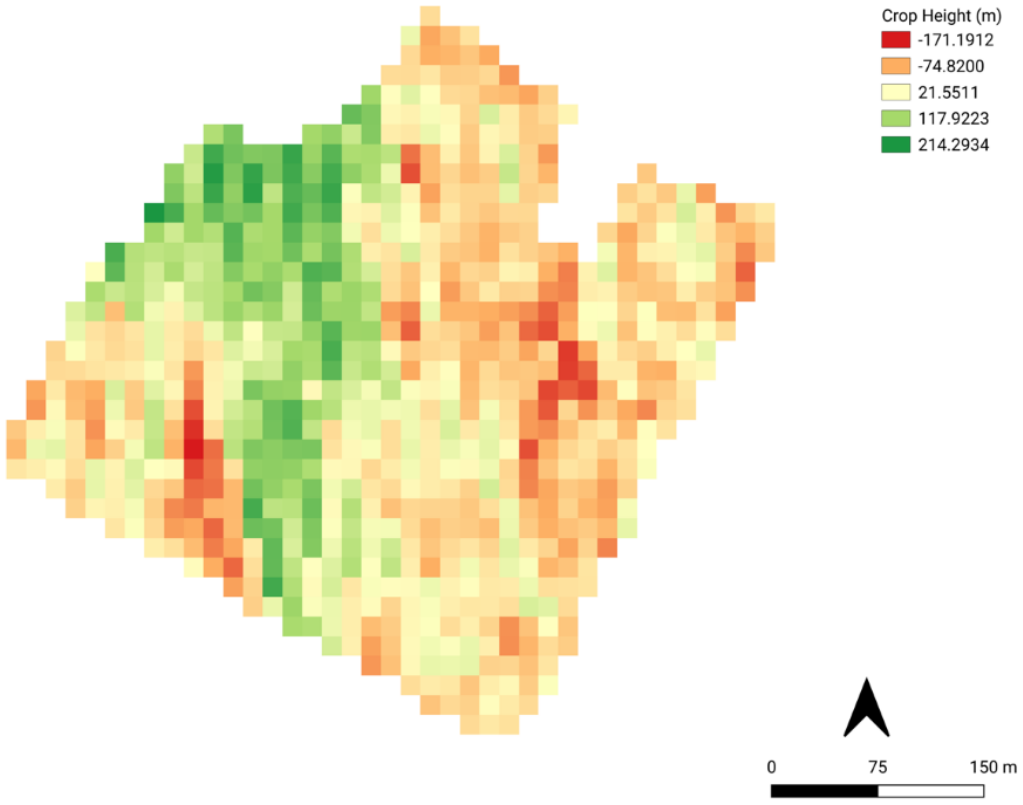

Figure 8: Map of crop heights derived from the June 15th Sentinel-1 imagery.

September 19th Sentinel-derived crop heights experienced a similar skewed distribution of values to that of June 15th crop heights with the majority of values being negative. Mean crop height value from the September 19th DSM minus the May 30th DTM (Figure 11) was –43.449.4 m (Figure 9). When Sentinel-derived crop heights were compared to the 11 measured crop heights (Figure 10), the calculated mean residual was 99.9 m, minimum residual was 31.0 m, maximum residual was 200.4 m, and standard deviation was 64.1 m. RMSE of the Sentinel data-derived values was 117.1 m. The location of the smallest residual value (31.0 m) was located in the southeastern section of the study area and the largest residual value (200.4 m)

was located in the northeast corner. When residual errors of the June 15th and September 19th Sentinel crop height values were compared, it was found that the difference between them was statistically significant (p=0.036).

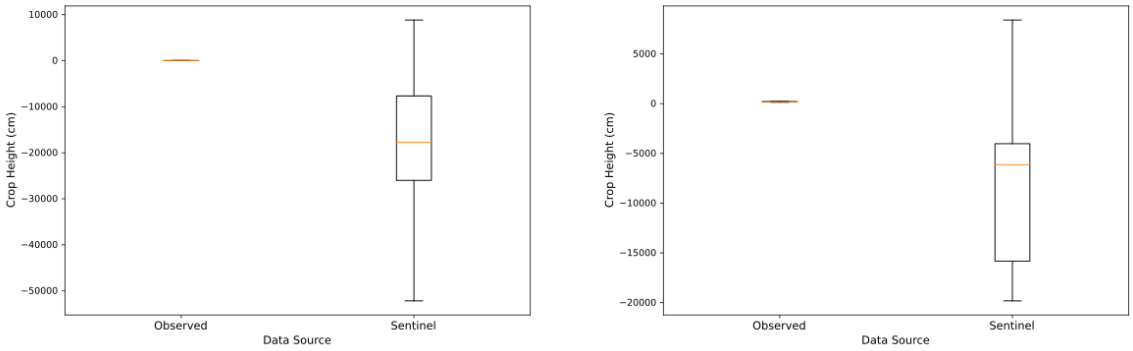

Figure 9: (Left) Distribution of crop height values between the observed data and Sentinel-derived data for the June 15, 2018 data collection (Right) Distribution of crop height values between the observed data and Sentinel-derived data for the September 19, 2018 data collection.

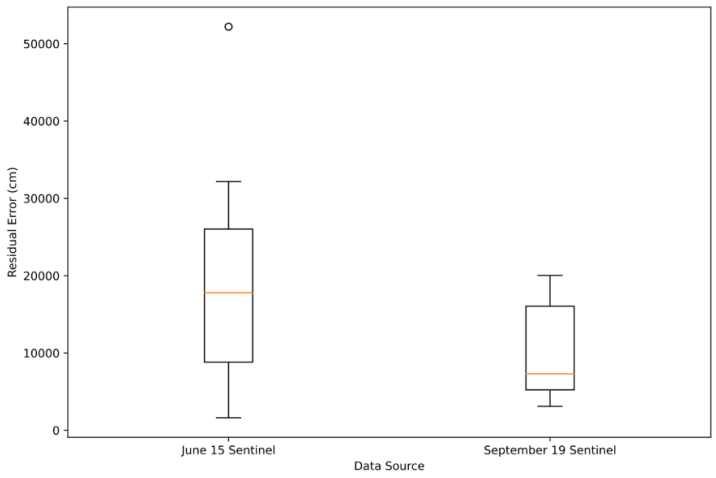

Figure 10: Distribution of crop height residual errors from the accuracy assessments performed on the Sentinel-derived crop height values for June 15, 2018 and September 19, 2018.

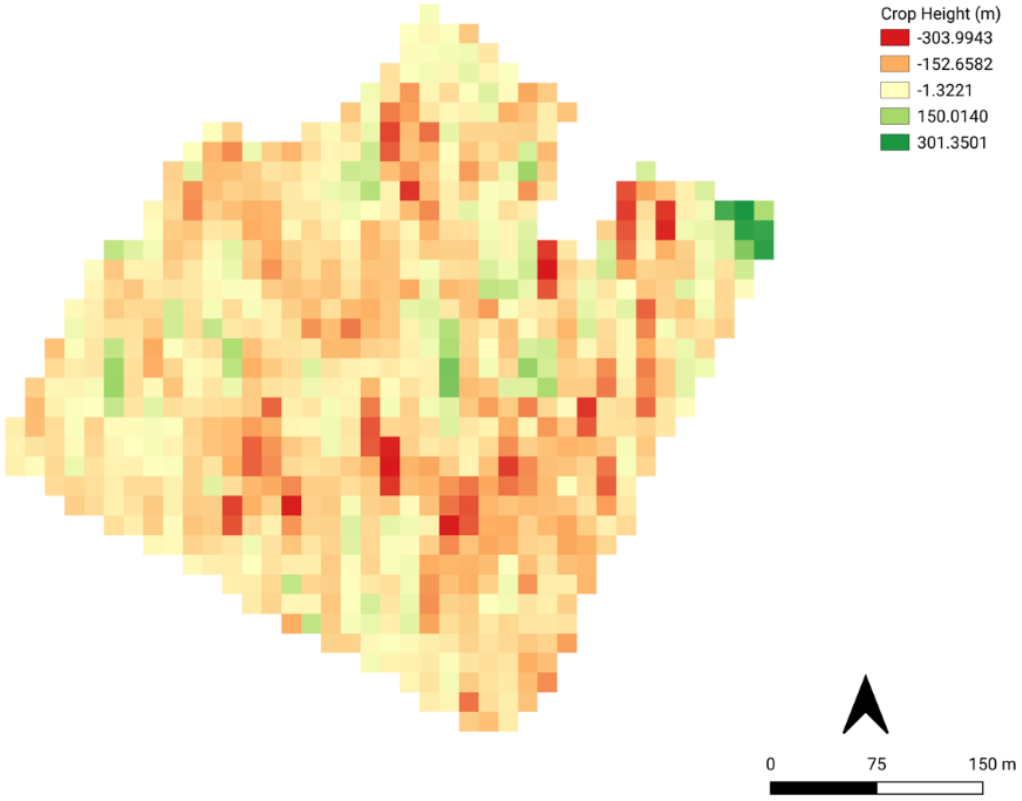

Figure 11: Map of crop heights derived from the September 19th Sentinel-1 imagery.

1.3.2 Leaf Area Index

Two methods were used to estimate LAI: regression, and an approach based on the fractional vegetation cover (Choudhury et al., 1994). Using Exploratory Regression in ArcGIS to identify the top ten ordinary least squares regression models and then sub-selecting the one with the combined lowest variance inflation factor and statistically significant coefficients.. Using the UAV based data resulted in the following equation:

$$LAI_{RPAS} = 1.507549 - 0.014304DjiGreen * +0.012894DjiBlue$$
$$* +0.000051ParrGreen * -0.000022ParrRedEdge + 1.640283NDVI$$
$$* +0.001021Aspect + 0.185593Height *$$

where DjiGreen and DjiBlue were pixel values from the green and blue bands respectively collected by the Zenmuse X3 sensor, ParrGreen and ParrRedEdge were pixel values from the green and red edge bands respectively collected by the Parrot Sequoia sensor, and NDVI, Aspect and Height were the calculated metrics defined in (Table 2). An asterisk beside a variable indicates statistical significance ($p<0.01$).

The R^2 value for the LAI_{RPAS} equation was 0.194 with an adjusted R^2 of 0.155. Variables with the highest VIF value in the equation were DjiGreen and DjiBlue with values of 13.230 and 13.898 respectively, which were most likely caused by spatial similarity in the data. The remaining variables all had VIF values less than 7.5, which is the recommended VIF threshold of the Exploratory Regression tool. The regression equation was generated by the Exploratory Regression tool using all of the observed LAI measurements which had the potential to cause over-fitting or bias. To test if the regression equation was created through an unbiased process, a spatial k-fold cross-validation test was performed using the predictor variables from the chosen LAI_{RPAS} equation and the observed LAI measurements. A spatial 10-fold cross-validation was conducted that yielded an average adjusted R^2 value of 0.156. Since the adjusted R^2 value for the selected regression equation (0.155) was almost identical to the average adjusted R^2 from the cross-validation, the Exploratory Regression tool did not overfit the regression equation to the observed data.

Performing the same process with data acquired by Sentinel yielded the following equation:

$$LAI_{Sentinel} = 2.542458 - 0.001272Aspect + 0.001834Height * +0.094537NDVI$$

where NDVI, Aspect and Height were the calculated metrics defined in Table 2. The R^2 value for the $LAI_{Sentinel}$ equation was 0.056 with an adjusted R^2 value of 0.036. All three variables had a VIF underneath the recommended 7.5 threshold with the highest VIF value being 1.110. A spatial 10-fold cross-validation was performed on the selected Sentinel regression equation and yielded an average adjusted value of 0.074.

Each regression was then applied on a cell-by-cell basis to both RPAS and Sentinel data to generate a continuous surface of RPAS (9 cm) estimated and Satellite (10 m) estimated LAI values, which could be compared against the 153 field observations and the field-mean LAI observation of 2.29. The LAI values generated from the RPAS data (Figure 12 and Figure 13b) had a mean value of 2.28, minimum value of 1.36, maximum value of 3.43, and a standard deviation of 0.40. When compared against the mean LAI of 153 field-measured locations, a mean residual of 0.67, minimum residual of 0.01, maximum residual of 1.99, and a standard deviation of the residuals of 0.46 were obtained with the LAI_{RPAS} yielding an RMSE of 0.81.

The regression derived LAI values using Sentinel data were applied against the 22 image pixels that corresponded to field-based LAI measurements. The $LAI_{Sentinel}$ (Figure 12 and Figure 13d) derived a mean value of 2.27, minimum value of 1.72, maximum value of 2.64, and a standard deviation of 0.25. When the regression data was compared against those

22 measurements, the mean residual was 0.45, minimum residual was 0.03, maximum residual was 1.25, and standard deviation of the residuals was 0.34. The raster had an RMSE of 0.56. While the three points that contained the highest residual values were all located in the north-west of the study area, the residuals showed no spatial trend.

When we assessed our second approach to estimate LAI based on Choudhury et al. (1994) (Figure 12 and Figure 13c), the RPAS estimated mean LAI across our measurement points was 2.43, minimum value of 1.65, maximum values of 3.72, and a standard deviation of 0.55. These values were both higher than the regression approach and farther from the observed values compared to the regression-based approach. The residuals had a mean of 0.74, a minimum of 0.01, a maximum of 2.55, and a standard deviation of 0.66. The RMSE of the Choudhury et al. (1994) approach was 0.99, which was almost twice that obtained by regression (0.56). When the means of the RPAS regression and Choudhury et al. (1994) LAI values were compared, it was found that there was a statistically significant difference between them ($p<0.01$).

LAI estimated values using the Choudhury et al. (1994) equation and Sentinel imagery (Figure 12 and Figure 13d) derived the same mean LAI value of 2.43 when rounded to two decimal places. Again, the range of values were higher relative to the RPAS estimated values using the Choudhury et al. (1994) equation with a minimum value of 2.14, maximum value of 2.66, and standard deviation of 0.13. Residuals had a mean of 0.45, minimum of 0.01, maximum of 1.21, and standard deviation of 0.33. The RMSE of the Choudhury et al. (1994) approach compared to field observations was 0.56, which matched the RMSE obtained from the regression approach applied to the RPAS data. Similar to the RPAS LAI means, the mean

of the Sentinel regression and Choudhury et al. (1994) LAI values were found to be statistically different (p=0.013).

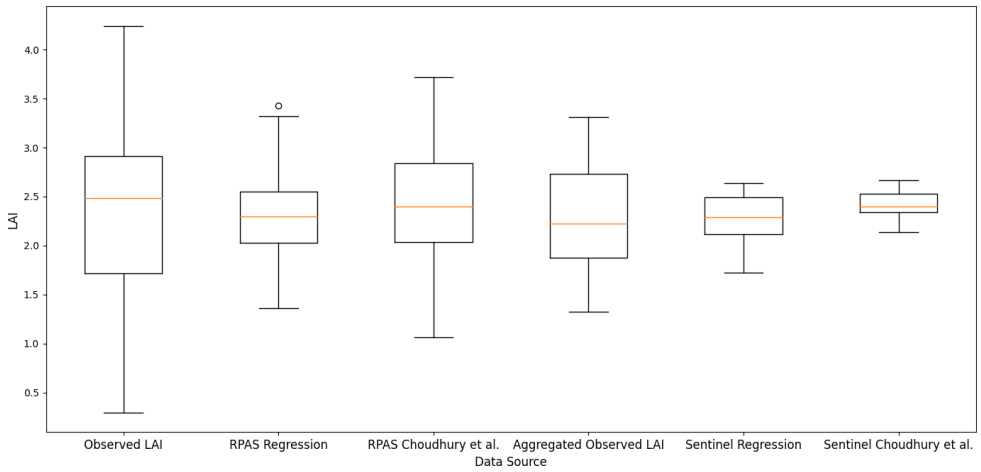

Figure 12: Distribution of RPAS and Sentinel estimated LAI values obtained by field observation, regression, and fraction of vegetation cover (Choudhury et al. 1994) for September 19, 2018.

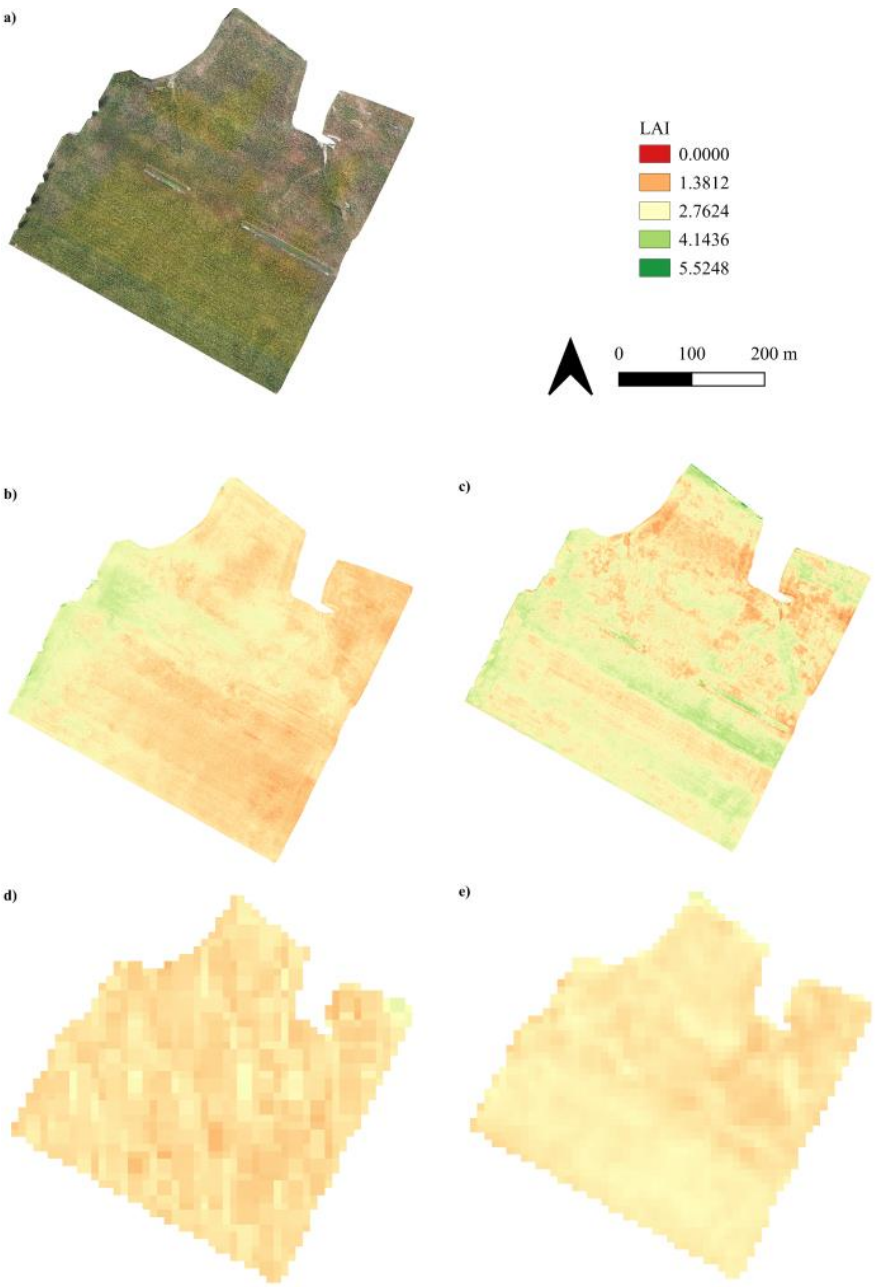

Figure 13: a) RGB imagery of the study area acquired by the RPAS on September 19, 2018, b) LAI values throughout the study area calculated from the RPAS regression equation, c) LAI values throughout the study area calculated from the RPAS Choudhury et al. (1994) equation, d) LAI values throughout the study area calculated from the Sentinel regression equation, e) LAI values throughout the study area calculated from the Sentinel Choudhury et al. (1994) equation.

Given the differences in the resolution of the RPAS (9 cm) and the Sentinel (10 m) data, a direct comparison with the field observations required aggregating the RPAS estimated LAI values to the same pixels used in the Sentinel derived LAI values. After the RPAS LAI values were aggregated, the difference between the regression and Choudhury et al. (1994) mean values remained statistically significant ($p=0.017$). The difference between the RPAS and Sentinel regression mean values and between the RPAS and Sentinel Choudhury et al. (1994) mean values were both not statistically significant with p-values of 0.71 and 0.11 respectively. Aggregating the RPAS LAI estimates reduced the RMSE for both the regression and Choudhury et al. (1994) approaches. The regression RMSE decreased from 0.81 to 0.42 and the Choudhury et al. (1994) RMSE decreased from 0.99 to 0.66. These aggregated RPAS derived LAI values yielded a lower level of error, relative to the field observations, compared to those obtained from the Sentinel data (Figure 14).

1.3.3 Crop Simulation Modelling

The DSSAT-CERES-Maize model generated results for a number of crop phenology metrics from the five crop growth simulations. The generated phenology metrics that were of interest for this study were LAI, canopy height, and yield across the 182 simulated growing days. The model indicated that the simulated crops were ready for harvest on the 126^{th} day (September 16, 2018), which indicated that the phenology metrics for the remaining 56 days were static. While the five simulations all had slightly different soil layer properties in their configuration files, they all produced the same results for LAI, canopy height, and yield. Since there was no difference between the results, the results of only one simulations were used..

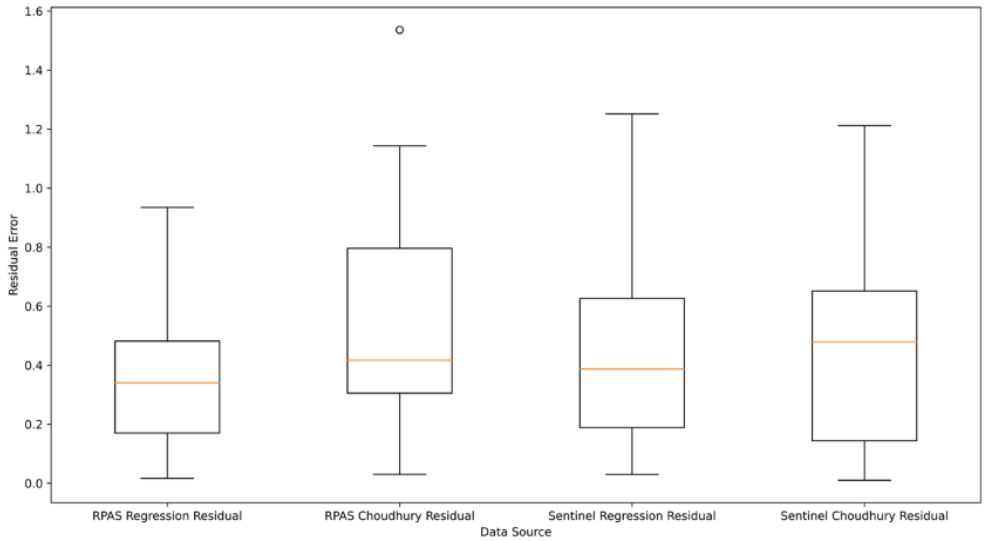

Figure 14: Comparison of residual errors from the RPAS-derived LAI value accuracy assessment to the residual errors from the Sentinel-derived LAI value accuracy assessment. Both accuracy assessments were performed with 22 aggregated observed LAI measurements.

The model simulated the beginning of non-zero LAI to be on the 13th day of the growing season (May 26, 2018) with a value of 0.01 and maximum LAI on the 69th day (July 21, 2018) with a value of 2.76. LAI then decreased daily until it reached a value of 1.12 on the 121st day (September 11, 2018) where it did not change for the rest of the simulation. The first non-zero LAI day was two days after the simulated emergence day of maize plants and the final LAI value of the growing season was one day before the crops ended their simulated grain filling stage, and four days before they reached their simulated full maturity. Simulated canopy height was the metric selected to represent crop heights for the model and will be referred to as the "crop height". The first non-zero crop height was 0.01 metres on the 13th day of the growing season similarly to the first non-zero LAI day. The crop height values followed an

exponential trend until reaching the maximum value of 1.6 m on the 55th growing day (July 7, 2018). Once the maximum crop height value was reached, the value stayed the same throughout the rest of the growing season.

While crop height and LAI values had similar dates for their significant changes, simulated crop yield was quite different due to maize grain production occurring later in the maize growth cycle. The first simulated crop yield (287 kg/ha) occurred on the 84th day of the growing season (August 5, 2018), which was also the beginning of the simulation's grain filling growth stage. The value increased rapidly in a linear trend between the 84th day and the 121st day (September 11, 2018) where the simulation reached its maximum crop yield value of 10183 kg/ha. Simulated crop yield continued to the maximum value of 10183 kg/ha until the end of the growing season. The maximum simulated crop yield value was 1952 kg/ha less than the measured crop yield of 12135 kg/ha that was reported by the farmer.

1.3.4 Comparison of Observations to RPAS and Crop Simulation Model Outputs

Results from the RPAS crop height and LAI calculations, as well from the CSM, were compared to further evaluate the utility of RPAS estimated crop characteristics. The relative accuracy of RPAS estimates was compared to a parameterized but uncalibrated crop model. RPAS-derived results used were from the June 15th, July 14th, and September 19th acquisitions for both LAI and crop height. The value representing each date for the metrics was calculated by averaging the value at each of the measured locations similarly to what was done in the earlier result sections (See sections 1.3.2 and 1.3.3). CSM results from the same dates were extracted to match the RPAS results. Finally, the observed measurements for both crop heights

and LAI were averaged on a field-scale so that two crop height measurements (June 15th and September 19th) and one LAI measurement (September 19th) were used in the comparison.

RPAS-derived crop heights were found to all be higher than both the CSM and observed values throughout the growing season (Figure 15). The closest RPAS values to the CSM was found to be from the July 14th points where the RPAS had a value of 2.34 m and the CSM had a value of 1.60 m. When the RPAS and CSM values were compared to the observed crop height measurements, the CSM crop height for June 15th was almost identical to the observed measurement with a value of 0.32 m to 0.43 m, respectively, while RPAS estimated a height of 1.18 m. The other observations, collected on September 19th, did not have as close of a RPAS or CSM value as the June 15th measurement did and instead deviated from each source by approximately the same amount. CSM underestimated the crop height with a value of 1.60 m compared to the observed value of 1.97 m, while RPAS overestimated the crop height with a value of 2.41 m.

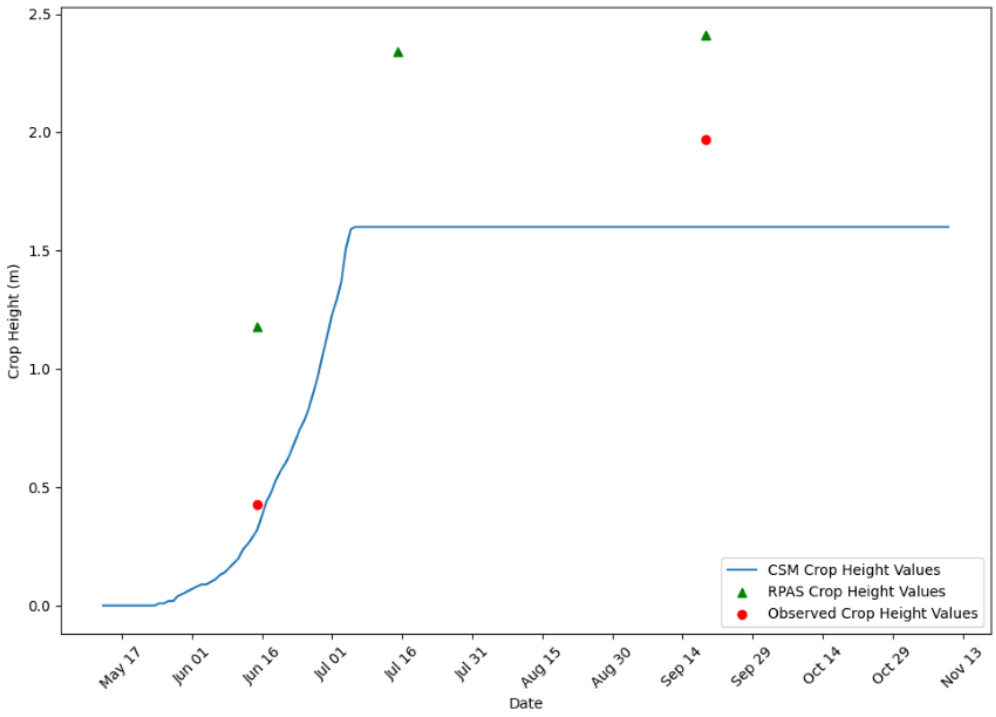

Figure 15: Comparison between crop height values derived from the RPAS (green) and CSM (blue) to the observed crop height measurements (red).

Comparison between RPAS LAI results and observed LAI (Figure 16) showed that regression LAI values were higher than the CSM values across all three dates, with the smallest difference occurring on July 14th where the regression had a value of 3.06 and the CSM had a value of 2.52. Choudhury et al. (1994) values had a slightly different trend in which they were higher than CSM values for both the June 15th and September 19th, but lower on July 14th. The date with the smallest difference between the Choudhury et al. (1994) and CSM LAI was on June 15th where the values were 1.28 and 2.52, respectively. When calculated September 19th LAI values were compared to observed LAI , the regression yielded the least different in LAI with a value of 2.28 compared to the observed value of 2.29. Coincidentally, the Choudhury

et al. (1994) value was also close to the observed measurement with a value of 2.43. However, while RPAS-derived LAI values were close to observed LAI, CSM underestimated with an LAI value of 1.12, which was approximately 50% less than the observed.

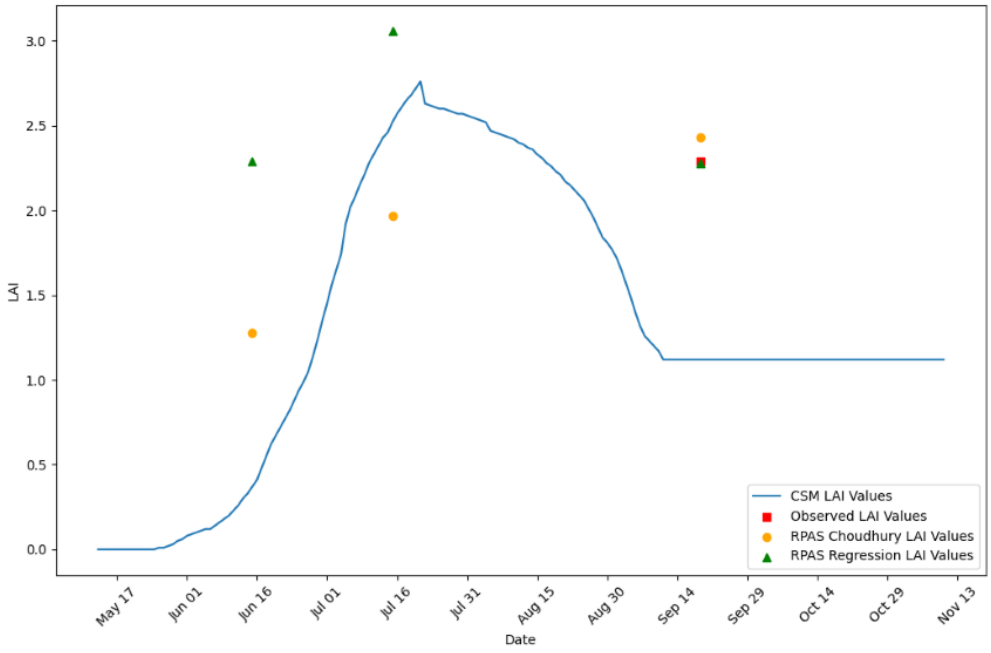

Figure 16: Comparison between LAI values derived from RPAS using the Choudhury et al. (1994) (orange), regression (green), LAI values derived from the CSM (blue), and the observed LAI measurements (red).

It is clear that CSM is capable of providing realistic crop height values during the beginning of the growing season but stagnates once it reaches a specific height. This stagnation may have been caused by either the cultivar configuration indicating a final crop height stage, or the model was unable to factor in the natural shrivelling of the plant, which would lead to a decreased crop height. Another potential cause may be the CSM having predetermined thresholds for growth metrics including crop heights to prevent unsustainable or unrealistic

growth rates regardless of input configurations. While LAI had a similar stagnated trend, it occurred much later in the season after a period of decreasing LAI but still under predicted LAI when compared to observed measurements. This suggests that simulated LAI values may have experienced a sudden decrease in LAI due to the cultivar configuration as well. Overall, both the simulated crop height and LAI values derived through the CSM moderately coincided with the RPAS-derived values and the observed measurements.

1.4 Discussion

1.4.1 Crop Height Comparisons

It was expected that September 19th RPAS estimated crop height values would be significantly closer to observed measurements than the June 15th RPAS estimates, due to the crop canopy being larger and easier to detect. However, the residual error was similar for both dates. Similarly, while some issues in the June 15th RPAS crop height estimates were expected, due to smaller, more sparse crop canopies, the expectation was that crop heights would be underestimated and would be closer to bare earth values (Grenzdörffer, 2014). This was not found in the results indicating other sources of error were present.

The likely cause of error in crop height results was an inaccurate DTM, which can cause significant inaccuracies in raster crop height calculations as well as other phenology metrics including biomass (Grenzdörffer, 2014; Wang et al. 2016). To determine if the DTM may have been the cause for inaccuracies in derived crop heights, the difference between the DSMs was calculated to show the change in crop height between the two dates. The mean difference between the two DSMs was 1.58 m, which when compared to the mean difference between the observed crop height measurements of 1.53 m suggests that the DSMs only

deviated from the observed measurements by 5 cm. While it is difficult to determine the accuracy of the DTM without observed elevation measurements, there is an obvious discrepancy between the accuracies of products that were generated using the DTM and those that were generated without it.

Existing studies estimating maize crop heights using RPAS have often shown high accuracy results with SfM-MVS (e.g., Bendig et al., 2014; Li et al., 2016; Ziliani et al., 2018) as well as with LiDAR (e.g., Luo et al., 2016; Wang et al., 2016). The error in crop heights was often found to be less than 1 m for both RGB optical and LiDAR sensors when flown at both high and low altitudes (De Souza et al. 2017; Holman et al., 2015; Ziliani et al., 2018), which was much more accurate than our results. A potential cause for the difference in accuracies may be the total area over which the studies were performed. Total area was often not reported in relevant studies and when it was reported, the area was often a small plot or section of a farm field (e.g., Gómez-Candón et al., 2014; Holman et al., 2016; Matthews and Jensen, 2013). While performing research at a plot scale is often more feasible for RPAS applications, it can artificially reduce the natural variation and potential error that would occur when observing an entire field.

Crop height values derived from Sentinel-1 were considerably inaccurate when compared to both the observed and RPAS-derived crop heights. While it was expected that the Sentinel-1 crop heights would be less accurate than RPAS estimates, the results deviated from observed crop heights by up to several hundred metres while also consisting of negative-value crop heights. Previous work has warned of the limitations of using interferometry for plant growth monitoring due to decorrelation occurring between the pairs of data as plant structure

change (Ballester-Berman et al., 2005; Engdahl et al., 2001; Pichierri et al., 2018). However, work done by Gomez-Dans et al. (2005) produced moderately accurate results of wheat crop heights when testing with multiple incidence angles in an indoor setting. Canisius et al. (2018) found a strong relation between observed and estimated crop heights for canola (0.90) and wheat (0.91) by estimating crop heights with a regression equation generated from Radarsat-2 imagery and observed measurements. While work done by Gomez-Dans et al. (2005) and Canisius et al. (2018) showed that deriving crop heights from interferometry was possible, both had access to multi-incidence angle data to determine a suitable incidence angle for their study, which was not available in our study.

1.4.2 Leaf Area Index Comparisons

The distribution of LAI data indicated that calculated LAI values from regression followed a stronger positive linear pattern than the Choudhury et al. (1994) approach. The lower RMSE for the regression relative to the Choudhury et al. (1994) approach for RPAS was expected since the raster was able to accommodate the influence of site-specific features at a higher resolution approach. However, it was unexpected that the regression and Choudhury et al. (1994) approaches would obtain the same RMSE for Sentinel data. A potential reason for the two Sentinel methods having almost identical RMSE values may have been due to the fact that both the regression and Choudhury et al. (1994) are heavily influenced by the same NDVI values. While the RPAS LAI regression values are influenced by NDVI and variables such as imagery band values that have the potential to cause increased variation, the Sentinel LAI regression values are only based on NDVI, aspect, and crop height. This similarity in input variables paired with a lower chance for variation caused by the coarse pixel resolution of

Sentinel imagery is the likely cause for similarity in RMSE values. It was also expected that RPAS would perform better than Sentinel data, however, this varied by the LAI estimation method used. When a regression-based approach was used, the RPAS data, aggregated to the same 10 m resolution of Sentinel data, had a lower RMSE (RPAS = 0.42, Sentinel = 0.56). In contrast, when the Choudhury et al. (1994) approach was used, the Sentinel data derived a lower RMSE (0.56) compared to the aggregated RPAS data RMSE (0.66). While the aggregation of RPAS Choudhury et al. (1994) LAI values lowered the RMSE value of the method, the influence of outlier data may have still caused the aggregated values to have a higher error than expected. Similarly, aggregated RPAS data may have also experienced a higher error due to the inherent variability of the data in its non-aggregated form influencing the averaging.

Use of RPAS for LAI calculations in Ontario was limited, possibly due to the novelty of the technology. However, several studies using satellite technologies have been performed. Corn LAI estimations were calculated using Landsat 5 and 7 multispectral satellite data by Liu et al. (2012). Estimates were calculated from regressions models that had similar inputs to the regressions performed in this study including NDVI and SAVI, as well as other vegetation indices. Averaged RMSE of the estimates generated by their regressions was found to be 0.65, which was higher than our regression RMSE values and close to the RMSE of the aggregated Choudhury et al. (1994) in our study (Liu et al., 2012). Shang et al. (2015) used imagery from the RapidEye (RapidEye AG) optical multispectral satellite to estimate LAI (referred to as plant area index) of spring wheat and canola. Regression equations were generated from vegetation indices similar to Liu et al. (2012). RMSE values for the selected best performing

equations were similar to the values in our study with an RMSE of 0.6-0.8 for spring wheat LAI and 0.4-0.6 for canola (Shang et al. 2015).

Other studies performed in Ontario, as well as the rest of the world, showed better performing LAI estimations than ours when using airborne Light Detection and Ranging (LiDAR) for maize (RMSE = 0.28) (Li et al., 2015), RPAS optical data for vineyard canopies (RMSE = 0.24) (Matthews et al., 2013), and optical satellite for winter wheat (RMSE = 0.53) (Dong et al. 2016). However, other studies with similar techniques resulted in poorer results than ours including RPAS optical data for soybean (RMSE = 0.67) (Yang et al. 2017) and optical satellite for maize (RMSE = 0.65) (Liu et al. 2012). The variation in LAI estimation accuracies across the reviewed literature, as well as our study, indicates that regressions generated were influenced by factors such as data acquisition timelines, number of observed measurements, and study area size. These factors make effective accuracy comparisons between the LAI studies difficult.

The literature for calculating LAI using remote sensing were predominantly based on regression analysis due to its accessibility for many users and applications. While regression analyses can show strong relations in data and create accurate estimations, their applicability outside of a specific study are often limited. Studies that used LAI models, including the SAIL and PROSAIL models, often required more specific inputs but were applicable for calculating LAI outside of the original study. Duan et al. (2014) showed the effectiveness of pairing hyperspectral data collected using an RPAS with the PROSAIL model to calculate the LAI of maize resulting in an RMSE of 0.66. Similarly, Haboudane et al. (2002) used hyperspectral

data for modelling leaf chlorophyll for corn plants which was proposed as an alternative to LAI estimations when corn plants are in their early growing stages.

1.4.3 Comparison among Observed, RPAS, and CSM

One of the objectives of this research was to evaluate the influence of RPAS calibration on crop simulation model (CSM) performance. While some of the estimated crop height and LAI values deviated between RPAS and CSM, the trends were moderately consistent. For estimated LAI trends, the CSM, RPAS Choudhury et al. (1994), and RPAS regression values all increased between June 15th and July 14th, but only the CSM and RPAS regression followed a decreasing pattern between July 14th and September 19th while the RPAS Choudhury et al. (1994) values continued increasing. The different direction of the RPAS Choudhury et al. (1994) values may be due to the use of parameters calibrated from observed LAI measurements collected on September 19th. While the generated regression equation for the RPAS regression values was also based on observed September 19th LAI measurements, the regression also included factors such as crop height, which may have resulted in the trend of values differing from Choudhury et al. (1994) values. The influence of observed LAI measurement being used in both RPAS methods was clear when compared to the CSM LAI values around September 19th. While final LAI values of both RPAS methods were close to observed LAI, the CSM's were much lower. This may have been improved if the CSM utilized the RPAS-derived LAI values in its estimation. The use of LAI values as inputs for CSM has been studied and has shown to improve prediction accuracies when LAI values were accurately collected (Casa et al., 2012; Li et al., 2017; Tewes et al., 2020).

The comparison between the crop height methods indicated that the CSM performed better than the RPAS in the early-stage of crop growth. While it was expected that CSM would perform better at early-stage growth since smaller crops are harder to detect by remote sensing, the difference in crop height of 0.86 m was significant. Potential causes for the large overestimation of the RPAS crop heights may have been attributed to issues experienced with calculating RPAS crop heights (see section 1.4.4). While CSM crop height estimation for the early-stage June 15th was very accurate, the accuracy for the late-stage September 19th was less, and was similar to the accuracy of the RPAS on that date. The decreased accuracy and underestimation of the crop height from the CSM was potentially caused by the CSM reaching a maximum height of 1.6 m on July 7th and then remaining constant throughout the growing season. While this approach was most likely enforced by either the programming of the model or the cultivar used to match historical crop height measurements, it limited the ability for the CSM to estimate crop heights closer to the observed.

CSM results from this study have shown that the DSSAT-CERES-Maize model tended to underestimate both LAI and crop height during the late-growth stages. Since both crop LAI (e.g., Curnel et al., 2011; Tewes et al., 2020; Xiao et al., 2011) and crop height (e.g., Bendig et al., 2014; Grenzdörffer 2014; Ziliani et al., 2018) are key parameters in crop growth and yield, underestimation of those key parameters can result in lower crop yield estimates as was seen in this study. Since underestimation in the CSM values may have been caused by thresholds set by the DSSAT developers, there is potential that other models suffer from similar limitations resulting in a loss of simulated growing days and total crop yield estimation. The LAI and crop height estimates derived from the RPAS imagery could be, in this case, used to

mitigate this issue by increasing the underestimated CSM values and result in a more accurate crop yield prediction. Potential future improvements could also be done through sampling the crop height and LAI measurements and acquiring RPAS imagery at a more frequent rate throughout the growing season. An increase in sampling could allow for a better comparison between the RPAS, CSM and observed values during key growth stages and may help determine which growth stages are accurately estimated by RPAS and CSM.

1.4.4 Challenges with RPAS data collection

One goal of combining field measurements and remote sensing is to scale-out from plots to fields and regions (e.g., Yang et al., 2017; Zhao et al., 2016; Ziliani et al., 2018). When we applied our regression and Choudhury et al. (1994) approaches, the latter approach represented greater heterogeneity in LAI values across the study area relative to the regression approach. A qualitative comparison based on field experience suggests that this heterogeneity is more reflective of what was observed in the field and aligns more closely with interpretation of the optical image of the study area. Furthermore, RPAS results across all metrics show an east-west gradient due to error in crop height estimates that was not observed in the field and is likely inhibiting the performance of the RPAS results.

Perhaps one of the biggest issues affecting RPAS data acquisition quality and subsequent analyses is the presence of doming (e.g., Eltner and Schneider, 2015; James and Robson, 2014). The use and stitching of hundreds to thousands of images can compound errors related to radial distortion, which is present to some degree in the in-expensive cameras used on RPAS (James and Robson, 2014), which leads (primarily) to vertical inaccuracies in the data (Girod and Filhol, 2020). The reduction of this doming can be achieved through accurate

real-time kinematic (Stott et al., 2020), post-processed kinematic (Zhang et al., 2019), or the inclusion of GCPs (Girod and Filhol, 2020; Meinen and Robinson 2020). While the study site has been used to evaluate the effects of increasing the number of GCPs on vertical and horizontal accuracy (Meinen and Robinson 2020), this work commenced before the data collection initiatives of Meinen and Robinson (2020). A gap in GCP placement on the initial data collection date (May 30, 2018), which was used to generate the DTM, may have inhibited the performance of the RPAS results. In addition, because the study area was an active agricultural field, the placement of GCPs varied for each RPAS data collection campaign, which could have altered the location of small doming errors that cumulatively impacted the results. While satellite-based remote sensing has a host of factors affecting error creation in image acquisition, doming error is not one of them.

Another factor affecting RPAS data collection is associated with battery life and flight duration. The DJI Inspire 1 RPAS used in the study used a 4500 mAH battery that had a manufacturer estimate of approximately 18 minutes of flight time. Due to the size of the study area, high imagery overlap requirement, and wind interference, a full imagery acquisition of the study area required two to three full batteries to perform. The availability of battery power influenced the resolution of the imagery orthomosaics and DSMs due to the RPAS needing to be flown at a higher altitude to capture large enough areas to cover the full study area. While the resolutions of the imagery products at an altitude of 90m were sufficient for this study, image quality degrades at higher altitudes (Seifert et al., 2019).

In addition to challenges associated with battery life, time-of-day of image acquisition had a substantial effect on image quality. The imaging sensor experienced over exposure when

imagery was acquired between the hours of 11am to 1pm due to the reflection of incident solar radiation from bare earth. When imagery was collected later in the day (3:20pm, Figure 17), over exposure did not occur, colours were more apparent and distinguishable, and imagery had a higher level of contrast. The increased reflectivity not only exaggerated pixel values, but it also reduced the ability of the SfM-MVS software to derive orthomosaic and DSM products (Ortega-Terol et al., 2017).

Figure 17: (Left) Image acquired by the RPAS during high brightness conditions, (Right) Image acquired by the RPAS during normal brightness conditions

A final issue, which may have affected the quality of RPAS data, involves the impact of a rolling shutter on image acquisition. The RGB sensor on the Parrot Sequoia camera uses a rolling shutter which causes geometrical distortions in acquired imagery (Figure 18) (Žížala et al., 2019). These geometrical distortions are caused by features in the field of view changing

location while the shutter literally rolls open and closed (Liang et al., 2008). The movement in the field of view may be caused by the features being sensed moving or by the sensor moving, as is the case when a rolling shutter is mounted on an RPAS (Figure 18). The issue can be amplified by vibrations caused by the RPAS, whereby it was attempted to mitigate this effect using rubber dampeners mounted between the Parrot Sequoia and RPAS. The rolling shutter was present only in imagery acquired by the Parrot Sequoia RGB sensor and not in the multispectral sensors or the RGB imagery acquired by DJI Zenmuse X3 sensor, which all use a global shutter and have short exposure lengths. While the Zenmuse X3 sensor was used for the presented research, the issue is acknowledged since the Parrot Sequoia RGB sensor had a higher resolution camera than the DJI Zenmuse X3 and the Sequoia RGB has been used in a number of studies (e.g., Ahmed et al., 2017; Khaliq et al., 2019; Žížala et al., 2019).

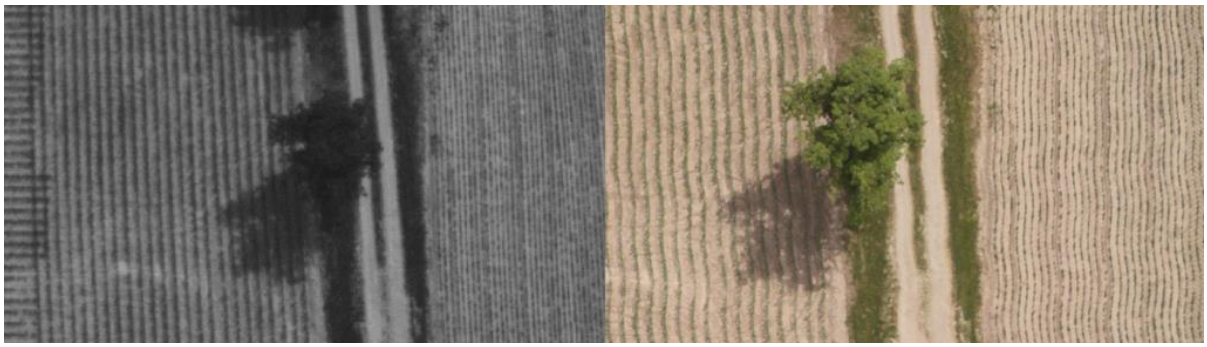

Figure 18: (Left) Image acquired with the multispectral sensor on the Parrot Sequoia that did not experience the rolling shutter effect, (Right) Image acquired with the RGB sensor on the Parrot Sequoia that experienced the rolling shutter effect.

1.4.5 Limitations of Sentinel

While the availability and coverage of Sentinel imagery greatly enhances its usability for many applications in agriculture, there are several limitations to the imagery when used in small

spatial extent applications such as performing in-field crop monitoring. Perhaps the greatest limitation of using both the Sentinel-1 and Sentinel-2 imagery at this scale was the spatial resolution of imagery. The width of measured corn plants in the field ranged between approximately 0.5 to 1.0 m meaning each 10 m pixel of Sentinel imagery contained between 100 to 200 corn plants (Figure 19). Generalization of the imagery reduces the effectiveness of creating physiological data of a crop such as the LAI and crop height values. The generalization across individual plants also prevents the analysis of outlier data in the form of either poor or healthy plants in the field, which removes the ability for an observer, or modeller, to determine what factors are influencing the growth of a crop in a very specific region. Since all products derived from the Sentinel imagery have a minimum resolution of 10 m, validating Sentinel data with in-field plot measurements is quite difficult since the extents of each pixel represents a large number of plants.

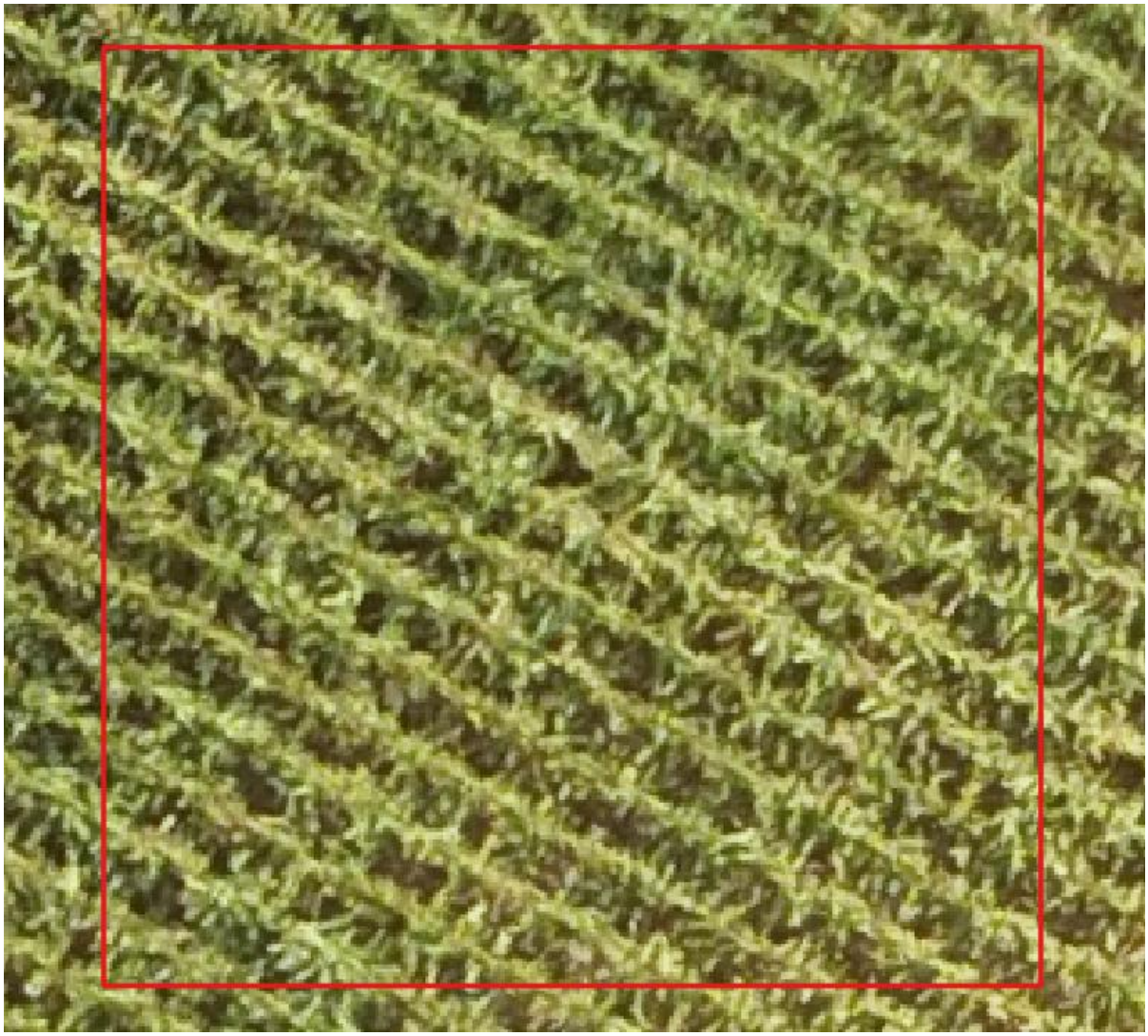

Figure 19: Example of the number of maize plants that are located in a single Sentinel-2 raster pixel (red box).

Cloud cover impacted the availability of Sentinel-2 imagery for this study due to one of the required datasets (June 8, 2018) experiencing almost full cloud coverage as well as shadow coverage across the remaining ground imagery. This issue causes loss of data and reduces the usefulness of imagery due to opaque clouds blocking out the ability for an optical

remote sensor to acquire relevant imagery (Eberhardt et al., 2016). While cloud coverage was only present in a single image, partially due to the matching RPAS acquisition dates being performed on days with clear weather, the impact of cloud coverage is quite apparent. This loss of data prevented an imagery comparison from being done with the RPAS imagery for the June 8th acquisition date.

1.4.6 Applications of Research

The research performed in this study provide an example of the benefits and limitations of RPAS systems for agricultural applications. While existing methods of remote sensing for agricultural applications, such as using satellite data, provide accurate results for some crop metrics, the spatial and temporal resolution of satellite observations limit their applications for in-field analyses. While in-field measurements are not always required or feasible due to studies being performed on a regional or national level, they may be necessary for both decision makers and agencies that work with decision makers. In Ontario, agencies that work with agricultural decision makers including the Ontario Ministry of Agriculture, Food, and Rural Affairs, have been helping farmers integrate precision agriculture technologies into their farming methods through the use of GPS-RTK-enabled combines, mobile proximal soil sensors, and RPAS (Ontario Ministry of Agriculture Food and Rural Affairs, 2015: Ontario Ministry of Agriculture Food and Rural Affairs, 2020). In the past, farmers and other decision makers have used RPAS for performing qualitative observations by capturing images or generating vegetation indices of a field and analyzing visually (Candiago et al., 2015; Khaliq et al., 2019). While the combination of decision maker expertise along with qualitative observations can provide insight into crop health, interpretations are often based on opinions

and are susceptible to bias. The quantitative data that can be extracted using RPAS provides a decision maker the ability to combine their expertise along with crop data to input into processes such as CSMs or other software which can assist in reinforcing decision making (Jones et al., 2003).

While research done in this study shows the potential for RPAS data to be used alongside CSMs, there is a need for further integration of RPAS into CSMs. The Simulateur mulTIdisciplinaire pour les Cultures Standard (STICS) (Brisson et al. 1998) CSM was developed to accept inputs of LAI values from external sources including remote sensing as validation for the simulated LAI values (Jégo et al., 2011). While this would have allowed for testing the RPAS data as a CSM input, STICS has become outdated which prevented it from being used in this study. A newer model, developed by the Climate Change, Agriculture, and Food Security Program, named the CCAFS Regional Agricultural Forecasting Toolbox (CRAFT) (Shelia et al., 2019), was designed to simulate crop growth and predict crop yield and uses gridded GIS data as inputs for parameters including weather, soil, and crop management (Shelia et al., 2019). The limitations of CRAFT are that it is a very new CSM that is still in its development stages as well as the scale at which the results are generated. Similar to other CSMs with GIS integration including GEPIC and AEGIS, the results are output at coarse resolutions with the highest resolution possible being 5 arc-minutes (6772 m). While a 5 arc-minute resolution may be appropriate for regional or national applications, it is difficult to use it for decision making on a field level and does not utilize the benefits of high resolution RPAS imagery. It is clear that existing CSM technologies do have capabilities that could be used to integrate RPAS data, but the methods are either outdated or currently not mature

enough. Improvements in the form of integrating validation data at field-scale or finer could allow for more streamlined modelling process with RPAS data which could lead to a wider adoption by decision makers.

1.5 Conclusion

Comparison of RPAS and Sentinel estimates of crop heights and LAI values, showed that the two technologies had significant difference in accuracy between crop heights but similar accuracies for LAI. The RPAS-derived crop heights for imagery acquisitions performed on June 15th, 2018 and September 19th, 2018 had significantly lower RMSE values of 193.6 cm and 161.3 cm when compared to the Sentinel-derived crop height with RMSE values of 223.4 m and 117.1 m. The derived LAI values were similar between the RPAS and Sentinel with RPAS RMSE values being 0.42 for the regression-based LAI and 0.66 for the Choudhury et al. (1994) method while the Sentinel RMSE values were 0.56 for both regression and Choudhury et al. (1994) methods.

Results of the comparisons between the methods indicate that the RPAS was significantly more accurate for crop height calculations when compared to the Sentinel, but the difference in accuracies between the estimated LAI values from both systems was minimal. The dominant reason for the inaccuracies in the Sentinel crop heights was caused by limitations in the interferometric process, used for generating crop heights, being prone to lower quality results when used in areas with growing vegetation (Chen et al., 2020). Although the results generated using the Sentinel-1 imagery were poor for this study, there are possibilities that interferometry using other radar missions could yield more accurate results. Free and publicly

available radar data that is acquired at a frequency appropriate for monitoring crop growth through a season is limited, but the use of appropriate proprietary radar data may improve the effectiveness of comparing crop heights between RPAS and satellite remote sensing. Alternatively, comparisons between crop height accuracies derived through RPAS SfM-MVS and other RPAS-compatible sensors including LiDAR may be more beneficial for studying the effectiveness of RPAS technologies in agricultural applications. Comparisons between these different sensors could quantify the accuracies while also providing insight into the cost-effectiveness of RPAS configurations, which could assist decision makers in determining the affordability and budget requirements of adopting RPAS technologies.

The results of the CSM showed that the simulated crop height values were similar to the observed crop height measurements with a difference of 11 cm at the beginning of the growing season. However, this relationship became weaker over the rest of the growing season potentially due to thresholds or limitations of the crop model. The CSM LAI values compared to the observed LAI measurement was found to considerably underestimate LAI with a difference of 1.17. When the CSM values throughout the growing season were compared to the RPAS derived crop height and LAI values, it was clear that the trends were similar but the values were not equal. There is potential for RPAS derived metrics, such as crop height and LAI, to be used as validation data for improving the accuracy of CSM results. Future work may be improved by collecting more RPAS imagery and observed measurements throughout the growing season to determine at which growth stages RPAS is effective at providing accurate crop physiology results.

Bibliography

Ahmed, O. S., Shemrock, A., Chabot, D., Dillon, C., Williams, G., Wasson, R., & Franklin, S. E. (2017). Hierarchical land cover and vegetation classification using multispectral data acquired from an unmanned aerial vehicle. *International Journal of Remote Sensing*,*38*(8–10), 2037–2052. https://doi.org/10.1080/01431161.2017.1294781

Baležentis, T., Galnaitytė, A., Kriščiukaitienė, I., Namiotko, V., Novickytė, L., Streimikiene, D., & Melnikiene, R. (2019). Decomposing Dynamics in the Farm Profitability: An Application of Index Decomposition Analysis to Lithuanian FADN Sample. *Sustainability*,*11*(10), 2861. https://doi.org/10.3390/su11102861

Ballester-Berman, J. D., Lopez-Sanchez, J. M., & Fortuny-Guasch, J. (2005). Retrieval of biophysical parameters of agricultural crops using polarimetric SAR interferometry. *IEEE Transactions on Geoscience and Remote Sensing*, *43*(4), 683–694. https://doi.org/10.1109/TGRS.2005.843958

Bendig, J., Bolten, A., Bennertz, S., Broscheit, J., Eichfuss, S., & Bareth, G. (2014). Estimating biomass of barley using crop surface models (CSMs) derived from UAV-based RGB imaging. *Remote Sensing*,*6*(11), 10395–10412. https://doi.org/10.3390/rs61110395

Blaschke, T., Hay, G. J., Kelly, M., Lang, S., Hofmann, P., Addink, E., Queiroz Feitosa, R., van der Meer, F., van der Werff, H., van Coillie, F., & Tiede, D. (2014). Geographic Object-Based Image Analysis - Towards a new paradigm. *ISPRS Journal of Photogrammetry and Remote Sensing*,*87*, 180–191. https://doi.org/10.1016/j.isprsjprs.2013.09.014

Brisson, N., Mary, B., Ripoche, D., Jeuffroy, M. H., Ruget, F., Nicoullaud, B., Gate, P., Devienne-Barret, F., Antonioletti, R., Durr, C., Richard, G., Beaudoin, N., Recous, S., Tayot, X., Plenet, D., Cellier, P., Machet, J.-M., Meynard, J. M., & Delécolle, R. (1998). STICS: a generic model for the simulation of crops and their water and nitrogen balances. I. Theory and parameterization applied to wheat and corn. *Agronomie*, *18*(5–6), 311–346. https://doi.org/10.1051/agro:19980501

Brown, M. B., & Forsythe, A. B. (1974). American Society for Quality The Small Sample Behavior of Some Statistics Which Test the Equality of Several Means Linked references are available on JSTOR for this article : The Small Sample Behavior of Some Statistics Which Test the Equality of Several. *Technometrics*, *16*(1), 129–132.

Bucksch, A., Atta-Boateng, A., Azihou, A. F., Battogtokh, D., Baumgartner, A., Binder, B. M., Braybrook, S. A., Chang, C., Coneva, V., DeWitt, T. J., Fletcher, A. G., Gehan, M. A., Diaz-Martinez, D. H., Hong, L., Iyer-Pascuzzi, A. S., Klein, L. L., Leiboff, S., Li, M., Lynch, J. P., … Chitwood, D. H. (2017). Morphological Plant Modeling:

Unleashing Geometric and Topological Potential within the Plant Sciences. *Frontiers in Plant Science*, *8*. https://doi.org/10.3389/fpls.2017.00900

Candiago, S., Remondino, F., De Giglio, M., Dubbini, M., & Gattelli, M. (2015). Evaluating multispectral images and vegetation indices for precision farming applications from UAV images. *Remote Sensing*,*7*(4), 4026–4047. https://doi.org/10.3390/rs70404026

Canisius, F., Shang, J., Liu, J., Huang, X., Ma, B., Jiao, X., Geng, X., Kovacs, J. M., & Walters, D. (2018). Tracking crop phenological development using multi-temporal polarimetric Radarsat-2 data. *Remote Sensing of Environment*, *210*(February 2017), 508–518. https://doi.org/10.1016/j.rse.2017.07.031

Casa, R., Varella, H., Buis, S., Guérif, M., De Solan, B., & Baret, F. (2012). Forcing a wheat crop model with LAI data to access agronomic variables: Evaluation of the impact of model and LAI uncertainties and comparison with an empirical approach. *European Journal of Agronomy*, *37*(1), 1–10. https://doi.org/10.1016/j.eja.2011.09.004

Chen, C. W., & Zebker, H. A. (2002). Phase unwrapping for large SAR interferograms: Statistical segmentation and generalized network models. *IEEE Transactions on Geoscience and Remote Sensing*,*40*(8), 1709–1719. https://doi.org/10.1109/TGRS.2002.802453

Chen, Y., Qiao, S., Zhang, G., Xu, Y. J., Chen, L., & Wu, L. (2020). Investigating the potential use of Sentinel-1 data for monitoring wetland water level changes in China's Momoge National Nature Reserve. *PeerJ*, *2020*(2). https://doi.org/10.7717/peerj.8616

Choudhury, B. J., Ahmed, N. U., Idso, S. B., Reginato, R. J., & Daughtry, C. S. . (1994). Relations between evaporation coefficients and vegetation indices studied by model simulations. *Remote Sensing of Environment*, *50*(1), 1–17. https://doi.org/10.1016/0034-4257(94)90090-6

Curnel, Y., de Wit, A. J. W., Duveiller, G., & Defourny, P. (2011). Potential performances of remotely sensed LAI assimilation in WOFOST model based on an OSS Experiment. *Agricultural and Forest Meteorology*, *151*(12), 1843–1855. https://doi.org/10.1016/j.agrformet.2011.08.002

De Souza, C. H. W., Lamparelli, R. A. C., Rocha, J. V., & Magalhães, P. S. G. (2017). Height estimation of sugarcane using an unmanned aerial system (UAS) based on structure from motion (SfM) point clouds. *International Journal of Remote Sensing*, *38*(8–10), 2218–2230. https://doi.org/10.1080/01431161.2017.1285082

Dong, T., Liu, J., Qian, B., Zhao, T., Jing, Q., Geng, X., Wang, J., Huffman, T., & Shang, J. (2016). Estimating winter wheat biomass by assimilating leaf area index derived from fusion of Landsat-8 and MODIS data. *International Journal of Applied Earth Observation and Geoinformation*, *49*, 63–74. https://doi.org/10.1016/j.jag.2016.02.001

Drusch, M., Del Bello, U., Carlier, S., Colin, O., Fernandez, V., Gascon, F., Hoersch, B., Isola, C., Laberinti, P., Martimort, P., Meygret, A., Spoto, F., Sy, O., Marchese, F., & Bargellini, P. (2012). Sentinel-2: ESA's Optical High-Resolution Mission for GMES Operational Services. *Remote Sensing of Environment*, *120*, 25–36. https://doi.org/10.1016/j.rse.2011.11.026

Duan, S. B., Li, Z. L., Wu, H., Tang, B. H., Ma, L., Zhao, E., & Li, C. (2014). Inversion of the PROSAIL model to estimate leaf area index of maize, potato, and sunflower fields from unmanned aerial vehicle hyperspectral data. *International Journal of Applied Earth Observation and Geoinformation*, *26*(1), 12–20. https://doi.org/10.1016/j.jag.2013.05.007

Dury, J., Schaller, N., Garcia, F., Reynaud, A., & Bergez, J. E. (2012). Models to support cropping plan and crop rotation decisions. A review. In *Agronomy for Sustainable Development* (Vol. 32, Issue 2, pp. 567–580). Springer. https://doi.org/10.1007/s13593-011-0037-x

Eberhardt, I., Schultz, B., Rizzi, R., Sanches, I., Formaggio, A., Atzberger, C., Mello, M., Immitzer, M., Trabaquini, K., Foschiera, W., & José Barreto Luiz, A. (2016). Cloud Cover Assessment for Operational Crop Monitoring Systems in Tropical Areas. *Remote Sensing*,*8*(3), 219. https://doi.org/10.3390/rs8030219

Eltner, A., & Schneider, D. (2015). Analysis of Different Methods for 3D Reconstruction of Natural Surfaces from Parallel-Axes UAV Images.*Photogrammetric Record*, *30*(151), 279–299. https://doi.org/10.1111/phor.12115

Engdahl, M. E., Borgeaud, M., & Rast, M. (2001). The use of ERS-1/2 Tandem interferometric coherence in the estimation of agricultural crop heights. *IEEE Transactions on Geoscience and Remote Sensing*,*39*(8), 1799–1806. https://doi.org/10.1109/36.942558

Environment and Climate Change Canada. (2018). *Station Results - Historical Data*. https://climate.weather.gc.ca/historical_data/search_historic_data_stations_e.html?searchType=stnName&timeframe=1&txtStationName=Roseville&searchMethod=contains&optLimit=yearRange&StartYear=1840&EndYear=2019&Year=2019&Month=6&Day=5&selRowPerPage=25

Fan, L., Gao, Y., Brück, H., & Bernhofer, C. (2009). Investigating the relationship between NDVI and LAI in semi-arid grassland in Inner Mongolia using in-situ measurements. *Theoretical and Applied Climatology*, *95*(1–2), 151–156. https://doi.org/10.1007/s00704-007-0369-2

Fortes, P. S., Platonov, A. E., & Pereira, L. S. (2005). GISAREG - A GIS based irrigation scheduling simulation model to support improved water use. *Agricultural Water Management*, *77*(1–3), 159–179. https://doi.org/10.1016/j.agwat.2004.09.042

Franke, J., & Menz, G. (2007). Multi-temporal wheat disease detection by multi-spectral remote sensing. *Precision Agriculture*, *8*(3), 161–172. https://doi.org/10.1007/s11119-007-9036-y

Gago, J., Douthe, C., Coopman, R. E., Gallego, P. P., Ribas-Carbo, M., Flexas, J., Escalona, J., & Medrano, H. (2015). UAVs challenge to assess water stress for sustainable agriculture. *Agricultural Water Management*, *153*, 9–19. https://doi.org/10.1016/j.agwat.2015.01.020

Galletti, C. S., & Myint, S. W. (2014). Land-use mapping in a mixed urban-agricultural arid landscape using object-based image analysis: A case study from Maricopa, Arizona. *Remote Sensing*, *6*(7), 6089–6110. https://doi.org/10.3390/rs6076089

Girod, L., & Filhol, S. (2020). Absolute coregistration and doming correction in adverse conditions, or how to retrieve snow depth from drone flights. *ISPRS Annals of the Photogrammetry, Remote Sensing and Spatial Information Sciences*, *5*(3), 375–379. https://doi.org/10.5194/isprs-Annals-V-3-2020-375-2020

Goldstein, R. M., & Werner, C. L. (1998). Radar interferogram filtering for geophysical applications. *Geophysical Research Letters*,*25*(21), 4035–4038. https://doi.org/10.1029/1998GL900033

Gómez-Candón, D., De Castro, A. I., & López-Granados, F. (2014). Assessing the accuracy of mosaics from unmanned aerial vehicle (UAV) imagery for precision agriculture purposes in wheat. *Precision Agriculture*,*15*(1), 44–56. https://doi.org/10.1007/s11119-013-9335-4

Grenzdörffer, G. J. (2014). Crop height determination with UAS point clouds.*International Archives of the Photogrammetry, Remote Sensing and Spatial Information Sciences - ISPRS Archives*, *40*(1), 135–140. https://doi.org/10.5194/isprsarchives-XL-1-135-2014

Haboudane, D., Miller, J. R., Tremblay, N., Zarco-Tejada, P. J., & Dextraze, L. (2002). Integrated narrow-band vegetation indices for prediction of crop chlorophyll content for application to precision agriculture.*Remote Sensing of Environment*, *81*(2–3), 416–426. https://doi.org/10.1016/S0034-4257(02)00018-4

Hämmerle, M., Höfle, B., Auernhammer, H., Anwar, M., Liu, D., Macadam, I., Kelly, G., Zhang, N., Wang, M., Wang, N., Schellberg, J., Hill, M., Gerhards, R., Rothmund, M., Braun, M., Eitel, J., Magney, T., Vierling, L., Brown, T., … May, S. (2016). Direct derivation of maize plant and crop height from low-cost time-of-flight camera measurements. *Plant Methods*, *12*(1), 50. https://doi.org/10.1186/s13007-016-0150-6

Holman, F. H., Riche, A. B., Michalski, A., Wooster, M. J., & Hawkesford, M. J. (2016). *remote sensing High Throughput Field Phenotyping of Wheat Plant Height and Growth*

Rate in Field Plot Trials Using UAV Based Remote Sensing. https://doi.org/10.3390/rs8121031

Jame, Y. W., & Cutforth, H. W. (1996). Crop growth models for decision support systems. *Canadian Journal of Plant Science*, *76*(1), 9–19. https://doi.org/10.4141/cjps96-003

James, M. R., & Robson, S. (2014). Mitigating systematic error in topographic models derived from UAV and ground-based image networks.*Earth Surface Processes and Landforms*, *39*(10), 1413–1420. https://doi.org/10.1002/esp.3609

Jégo, G., Pattey, E., Bourgeois, G., Drury, C. F., & Tremblay, N. (2011). Evaluation of the STICS crop growth model with maize cultivar parameters calibrated for Eastern Canada. *Agronomy for Sustainable Development*, *31*(3), 557–570. https://doi.org/10.1007/s13593-011-0014-4

Jones, C. L., Maness, N. O., Stone, M. L., & Jayasekara, R. (2004). Sonar and Digital Imagery for Estimating Crop Biomass. *ASAE/CSAE Annual International Meeting Meeting Paper No. 043061*, 1–13. https://www.researchgate.net/profile/Niels_Maness/publication/251757297_Sonar_and_Digital_Imagery_for_Estimating_Crop_Biomass/links/546a1c080cf2397f783011d8/Sonar-and-Digital-Imagery-for-Estimating-Crop-Biomass.pdf?origin=publication_detail

Jones, J. W., Hoogenboom, G., Porter, C. H., Boote, K. J., Batchelor, W. D., Hunt, L. A., Wilkens, P. W., Singh, U., Gijsman, A. J., & Ritchie, J. T. (2003). The DSSAT cropping system model. In *European Journal of Agronomy* (Vol. 18, Issues 3–4). https://doi.org/10.1016/S1161-0301(02)00107-7

Khaliq, A., Comba, L., Biglia, A., Aimonino, D. R., Chiaberge, M., & Gay, P. (2019). *remote sensing Comparison of Satellite and UAV-Based Multispectral Imagery for Vineyard Variability Assessment*. https://doi.org/10.3390/rs11040436

Kisekka, I., DeJonge, K. C., Ma, L., Paz, J., & Douglas-Mankin, K. (2017). Crop modeling applications in agricultural water management.*Transactions of the ASABE*, *60*(6), 1959–1964. https://doi.org/10.13031/trans.12693

Lazecký, M., Hlaváčová, I., Martinovic, J., & Ruiz-Armenteros, A. M. (2018). Accuracy of sentinel-1 interferometry monitoring system based on topography-free phase images. *Procedia Computer Science*,*138*, 310–317. https://doi.org/10.1016/j.procs.2018.10.044

Li, H., Chen, Z., Liu, G., Jiang, Z., & Huang, C. (2017). Improving winter wheat yield estimation from the CERES-Wheat model to assimilate leaf area index with different assimilation methods and spatio-temporal scales. *Remote Sensing*, *9*(3). https://doi.org/10.3390/rs9030190

Li, Z. T., Yang, J. Y., Smith, W. N., Drury, C. F., Lemke, R. L., Grant, B., He, W. T., & Li, X. G. (2015). Simulation of long-term spring wheat yields, soil organic C, N and water dynamics using DSSAT-CSM in a semi-arid region of the Canadian prairies. *Nutrient Cycling in Agroecosystems*, *101*(3), 401–419. https://doi.org/10.1007/s10705-015-9688-3

Liang, C. K., Chang, L. W., & Chen, H. H. (2008). Analysis and compensation of rolling shutter effect. *IEEE Transactions on Image Processing*, *17*(8), 1323–1330. https://doi.org/10.1109/TIP.2008.925384

Liu, H. L., Yang, J. Y., Drury, C. F., Reynolds, W. D., Tan, C. S., Bai, Y. L., He, P., Jin, J., & Hoogenboom, G. (2011). Using the DSSAT-CERES-Maize model to simulate crop yield and nitrogen cycling in fields under long-term continuous maize production. *Nutrient Cycling in Agroecosystems*, *89*(3), 313–328. https://doi.org/10.1007/s10705-010-9396-y

Liu, Jiangui, Pattey, E., & Jégo, G. (2012). Assessment of vegetation indices for regional crop green LAI estimation from Landsat images over multiple growing seasons. *Remote Sensing of Environment*,*123*, 347–358. https://doi.org/10.1016/j.rse.2012.04.002

Liu, Junguo, Fritz, S., van Wesenbeeck, C. F. A., Fuchs, M., You, L., Obersteiner, M., & Yang, H. (2008). A spatially explicit assessment of current and future hotspots of hunger in Sub-Saharan Africa in the context of global change. *Global and Planetary Change*, *64*(3–4), 222–235. https://doi.org/10.1016/j.gloplacha.2008.09.007

Mann, M. L., & Warner, J. M. (2017). Ethiopian wheat yield and yield gap estimation: A spatially explicit small area integrated data approach. *Field Crops Research*, *201*, 60–74. https://doi.org/10.1016/j.fcr.2016.10.014

Mathews, A., & Jensen, J. (2013). Visualizing and Quantifying Vineyard Canopy LAI Using an Unmanned Aerial Vehicle (UAV) Collected High Density Structure from Motion Point Cloud. *Remote Sensing*,*5*(5), 2164–2183. https://doi.org/10.3390/rs5052164

Matsushita, B., & Tamura, M. (2002). Integrating remotely sensed data with an ecosystem model to estimate net primary productivity in East Asia.*Remote Sensing of Environment*, *81*(1), 58–66. https://doi.org/10.1016/S0034-4257(01)00331-5

Meinen, B. U., & Robinson, D. T. (2020). Mapping erosion and deposition in an agricultural landscape: Optimization of UAV image acquisition schemes for SfM-MVS. *Remote Sensing of Environment*, *239*, 111666. https://doi.org/10.1016/j.rse.2020.111666

Menzies Pluer, E. G., Robinson, D. T., Meinen, B. U., & Macrae, M. L. (2020). Pairing soil sampling with very-high resolution UAV imagery: An examination of drivers of soil and nutrient movement and agricultural productivity in southern Ontario. *Geoderma*, *379*, 114630. https://doi.org/10.1016/j.geoderma.2020.114630

Mondal, P., Basu, M., & Bhadoria, P. B. S. (2011). Critical Review of Precision Agriculture Technologies and Its Scope of Adoption in India. *American Journal of Experimental Agriculture 1(3): 49-68, 2011*, *1*(3), 49–68.

Moulin, S., Bondeau, A., & Delecolle, R. (1998). Combining agricultural crop models and satellite observations: From field to regional scales. *International Journal of Remote Sensing*, *19*(6), 1021–1036. https://doi.org/10.1080/014311698215586

Nagamani, K., & Nethaji Mariappan, V. E. (2017). Remote Sensing, GIS and Crop Simulation Models – A Review K. *International Journal of Current Research in Biosciences and Plant Biology*, *4*(8), 80–92.

Nyang'Au, W. O., Mati, B. M., Kalamwa, K., Wanjogu, R. K., & Kiplagat, L. K. (2014). Estimating rice yield under changing weather conditions in kenya using ceres rice model. *International Journal of Agronomy*,*2014*. https://doi.org/10.1155/2014/849496

Ontario Ministry of Agriculture Food and Rural Affairs. (2015). *What's new in precision ag & soils?*http://www.omafra.gov.on.ca/english/crops/hort/news/hortmatt/2015/15hrt15a7.htm

Ontario Ministry of Agriculture Food and Rural Affairs. (2017). *Statistical Summary of Ontario Agriculture*. http://www.omafra.gov.on.ca/english/stats/agriculture_summary.htm

Ontario Ministry of Agriculture Food and Rural Affairs. (2020). *2020-21 OMAFRA Research Priorities*. https://www.uoguelph.ca/alliance/system/files/2020-21 OMAFRA Research Priorities - FINAL_1.pdf

Ortega-Terol, D., Hernandez-Lopez, D., Ballesteros, R., & Gonzalez-Aguilera, D. (2017). Automatic hotspot and sun glint detection in UAV multispectral images. *Sensors (Switzerland)*, *17*(10). https://doi.org/10.3390/s17102352

Oteng-Darko, P., Yeboah, S., Addy, S. N. T., Amponsah, S., & Danquah, E. O. (2013). Crop modeling: A tool for agricultural research – A review.*E3 Journal of Agricultural Research and Development*, *2*(1), 1–6. http://www.e3journals.org

Pasley, H. R., Huber, I., Castellano, M. J., & Archontoulis, S. V. (2020). Modeling Flood-Induced Stress in Soybeans. *Frontiers in Plant Science*, *11*, 62. https://doi.org/10.3389/fpls.2020.00062

Pastor-Guzman, J., Atkinson, P., Dash, J., & Rioja-Nieto, R. (2015). Spatotemporal Variation in Mangrove Chlorophyll Concentration Using Landsat 8. *Remote Sensing*, *7*(11), 14530–14558. https://doi.org/10.3390/rs71114530

Pichierri, M., Hajnsek, I., Zwieback, S., & Rabus, B. (2018). On the potential of Polarimetric SAR Interferometry to characterize the biomass, moisture and structure of agricultural crops at L-, C- and X-Bands. *Remote Sensing of Environment*, *204*(September 2017), 596–616. https://doi.org/10.1016/j.rse.2017.09.039

Pickering, N. B., Hansen, J. W., Jones, J. W., Wells, C. M., Chan, V. K., & Godwin, D. C. (1994). WeatherMan: A utility for managing and generating daily weather data. *Agronomy Journal*, *86*(2), 332–337. https://doi.org/10.2134/agronj1994.00021962008600020023x

Salo, T. J., Palosuo, T., Kersebaum, K. C., Nendel, C., Angulo, C., Ewert, F., Bindi, M., Calanca, P., Klein, T., & Moriondo, M. (2016). Comparing the performance of 11 crop simulation models in predicting yield response to nitrogen fertilization. *Journal of Agricultural Science*, *7*, 1218–1240. https://doi.org/10.1017/s0021859615001124ï

Seifert, E., Seifert, S., Vogt, H., Drew, D., van Aardt, J., Kunneke, A., & Seifert, T. (2019). Influence of drone altitude, image overlap, and optical sensor resolution on multi-view reconstruction of forest images. *Remote Sensing*, *11*(10). https://doi.org/10.3390/rs11101252

Shang, J., Liu, J., Ma, B., Zhao, T., Jiao, X., Geng, X., Huffman, T., Kovacs, J. M., & Walters, D. (2015). Mapping spatial variability of crop growth conditions using RapidEye data in Northern Ontario, Canada. *Remote Sensing of Environment*, *168*, 113–125. https://doi.org/10.1016/j.rse.2015.06.024

Shapiro, A. S. S., & Wilk, M. B. (1965). An Analysis of Variance Test for Normality (Complete Samples). *Biometrika*, *52*(3/4), 591–611. www.jstor.org/stable/2333709

Shelia, V., Hansen, J., Sharda, V., Porter, C., Aggarwal, P., Wilkerson, C. J., & Hoogenboom, G. (2019). A multi-scale and multi-model gridded framework for forecasting crop production, risk analysis, and climate change impact studies. *Environmental Modelling and Software*, *115*, 144–154. https://doi.org/10.1016/j.envsoft.2019.02.006

Sparks, A. (2018). nasapower: A NASA POWER Global Meteorology, Surface Solar Energy and Climatology Data Client for R. *Journal of Open Source Software*, *3*(30), 1035. https://doi.org/10.21105/joss.01035

Statistics Canada. (2017). *Land Use*. https://www150.statcan.gc.ca/t1/tbl1/en/tv.action?pid=3210040601&pickMembers%5B0%5D=1.1126&cubeTimeFrame.startYear=2011&cubeTimeFrame.endYear=2016&referencePeriods=20110101%2C20160101

Stockle, C. O., Donatelli, M., Nelson, R., Stöckle, C. O., Donatelli, M., Nelson, R., Stockle, C. O., Donatelli, M., Nelson, R., Stöckle, C. O., Donatelli, M., Nelson, R., Stockle, C.

O., Donatelli, M., & Nelson, R. (2003). CropSyst, a cropping systems simulation model.*European Journal of Agronomy*, *18*(3–4), 289–307. https://doi.org/Pii S1161-0301(02)00109-0

Stott, E., Williams, R. D., & Hoey, T. B. (2020). Ground Control Point Distribution for Accurate Kilometre-Scale Topographic Mapping Using an RTK-GNSS Unmanned Aerial Vehicle and SfM Photogrammetry. *Drones*, *4*(3), 1AA+. https://link.gale.com/apps/doc/A638158684/AONE?u=uniwater&sid=AONE&xid=d3bb8785

Swain, K. C., Jayasuriya, H. P. W., & Salokhe, V. M. (2007). Suitability of low-altitude remote sensing images for estimating nitrogen treatment variations in rice cropping for precision agriculture adoption. *Journal of Applied Remote Sensing*, *1*(1), 1–11. https://doi.org/10.1117/1.2824287

Tewes, A., Hoffmann, H., Krauss, G., Schäfer, F., Kerkhoff, C., & Gaiser, T. (2020). New approaches for the assimilation of LAI measurements into a crop model ensemble to improve wheat biomass estimations. *Agronomy*, *10*(3), 446. https://doi.org/10.3390/agronomy10030446

Thorp, K. R., Wang, G., West, A. L., Moran, M. S., Bronson, K. F., White, J. W., & Mon, J. (2012). Estimating crop biophysical properties from remote sensing data by inverting linked radiative transfer and ecophysiological models. *Remote Sensing of Environment*, *124*, 224–233. https://doi.org/10.1016/j.rse.2012.05.013

Tubiello, F. N., Soussana, J.-F., & Howden, S. M. (2007). Crop and pasture response to climate change. *Proceedings of the National Academy of Sciences*, *104*(50), 19686–19690. https://doi.org/10.1073/pnas.0701728104

Tzouvaras, M., Danezis, C., & Hadjimitsis, D. G. (2020). Differential SAR Interferometry Using Sentinel-1 Imagery-Limitations in Monitoring Fast Moving Landslides: The Case Study of Cyprus. *Geosciences*,*10*(6), 236–261. https://doi.org/10.3390/geosciences10060236

Unigarro M., C. A., Jaramillo R., Á., & Flórez R., C. P. (2017). Evaluation of six leaf angle distribution functions in the Castillo ® coffee variety. *Agronomía Colombiana*, *35*(1), 23. https://doi.org/10.15446/agron.colomb.v35n1.60063

Wang, C., Nie, S., Xi, X., Luo, S., & Sun, X. (2016). Estimating the biomass of maize with hyperspectral and LiDAR data. *Remote Sensing*, *9*(1), 11. https://doi.org/10.3390/rs9010011

Welch, A. B. L. (1947). The Generalization of "Student's" Problem when Several Different Population Variances are Involved. *Biometrika*, *34*(1/2), 28–35. https://doi.org/10.2307/2332510

Xiao, Z., Liang, S., Wang, J., Jiang, B., & Li, X. (2011). Real-time retrieval of Leaf Area Index from MODIS time series data. *Remote Sensing of Environment, 115*(1), 97–106. https://doi.org/10.1016/j.rse.2010.08.009

Xiong, W., Skalsky, R., Porter, C. H., Balkovic, J., Jones, J. W., & Yang, D. (2016). Calibration-induced uncertainty of the EPIC model to estimate climate change impact on globalmaize yield. *Journal of Advances in Modeling Earth Systems, 8*, 1358–1375. https://doi.org/10.1002/2016MS000625.

Yang, G., Liu, J., Zhao, C., Li, Z., Huang, Y., Yu, H., Xu, B., Yang, X., Zhu, D., Zhang, X., Zhang, R., Feng, H., Zhao, X., Li, Z., Li, H., & Yang, H. (2017). Unmanned aerial vehicle remote sensing for field-based crop phenotyping: Current status and perspectives.*Frontiers in Plant Science, 8*, 1111. https://doi.org/10.3389/fpls.2017.01111

Yu, J. H., Ge, L., & Rizos, C. (2010). Technical report: SRTM DEM updating using selected InSAR DEM elevations based on coherence value selection method. *Journal of Applied Geodesy*, *4*(3), 157–165. https://doi.org/10.1515/jag.2010.015

Zhang, H., Aldana-Jague, E., Wilken, F., Vanacker, V., & Van Oost, K. (2019). Evaluating the potential of post-processing kinematic (PPK) georeferencing for UAV-based structure- from-motion (SfM) photogrammetry and surface change detection. *Earth Surface Dynamics*, *7*(3), 807. https://link.gale.com/apps/doc/A598158296/AONE?u=uniwater&sid=AONE&xid=26763517

Zhao, T., Stark, B., Chen, Y. Q., Ray, A., & Doll, D. (2016). More Reliable Crop Water Stress Quantification Using Small Unmanned Aerial Systems (sUAS). *IFAC-PapersOnLine*, *49*(16), 409–414. https://doi.org/10.1016/j.ifacol.2016.10.075

Zheng, H., Cheng, T., Zhou, M., Li, D., Yao, X., Tian, Y., Cao, W., & Zhu, Y. (2018). Improved estimation of rice aboveground biomass combining textural and spectral analysis of UAV imagery. *Precision Agriculture*, 1–19. https://doi.org/10.1007/s11119-018-9600-7

Ziliani, M. G., Parkes, S. D., Hoteit, I., & McCabe, M. F. (2018). Intra-season crop height variability at commercial farm scales using a fixed-wing UAV. *Remote Sensing*, *10*(12), 2007. https://doi.org/10.3390/rs10122007

Žížala, D., Minařík, R., & Zádorová, T. (2019). Soil Organic Carbon Mapping Using Multispectral Remote Sensing Data: Prediction Ability of Data with Different Spatial and Spectral Resolutions.*Remote Sensing*, *11*(24), 2947. https://doi.org/10.3390/rs11242947

Appendix A: Soil Analyses Performed

Table 3: Soil analysis performed on collected soil samples.

Soil Test	Units
Soil Moisture	%
Ammonium N	mg/kg dry
Nitrate N	mg/kg dry
Total Carbon	% dry
Inorganic Carbon	% dry
Organic Carbon	% dry
Organic Matter	% dry
Particle Distribution	%
Phosphorous (Extractable)	mg/L soil dry
Magnesium (Extractable)	mg/L soil dry
Potassium (Extractable)	mg/L soil dry
Manganese (Extractable)	mg/L soil dry
Zinc (Extractable)	mg/L soil dry
pH	-
Sulfur	% dry

Appendix B: Example of a GCP used during RPAS imagery acquisition

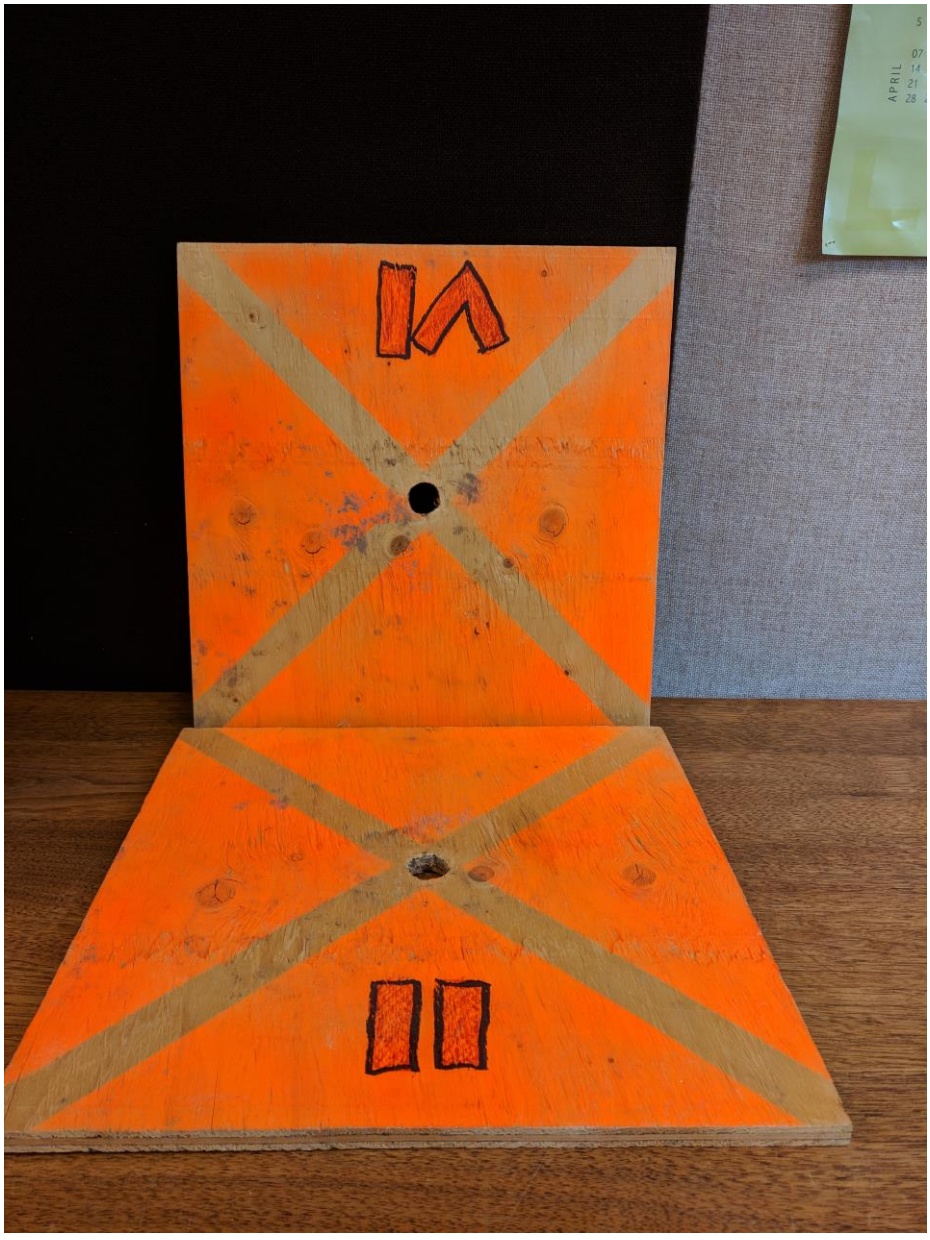

Figure B: Example of GCP used during the RPAS imagery acquisition.

Appendix C: List of IW SLC Datasets Used for Interferometry

Table C: Sentinel-1 datasets used for interferometry pairs.

Target Interferogram Date	IW SLC dataset pair used for interferogram formation	Time period between dataset acquisitions (days)	Baseline value (m)
May 1, 2018	• S1A_IW_SLC__1SDV_20180428T231611_20180428T231638_021674_025616_BAC7 (April 28, 2018) • S1A_IW_SLC__1SDV_20180510T231612_20180510T231639_021849_025BA5_7572 (May 10, 2018)	12	130
May 30, 2018	• S1A_IW_SLC__1SDV_20180522T231612_20180522T231639_022024_026137_4936 (May 22, 2018) • S1A_IW_SLC__1SDV_20180603T231613_20180603T231640_022199_0266C0_81CF (June 3, 2018)	12	33
June 8, 2018	• S1A_IW_SLC__1SDV_20180603T231613_20180603T231640_022199_0266C0_81CF (June 3, 2018) • S1A_IW_SLC__1SDV_20180615T231614_20180615T231641_022374_026C2C_0878 (June 15, 2018)	12	47

Target Interferogram Date	IW SLC dataset pair used for interferogram formation	Time period between dataset acquisitions (days)	Baseline value (m)
June 15, 2018	• S1A_IW_SLC__1SDV_20180615T231614_20180615T231641_022374_026C2C_0878 (June 15, 2018) • S1A_IW_SLC__1SDV_20180627T231615_20180627T231642_022549_027150_9A68 (June 27, 2018)	12	21
July 15, 2018	• S1A_IW_SLC__1SDV_20180709T231615_20180709T231642_022724_02766D_74C4 (July 9, 2018) • S1A_IW_SLC__1SDV_20180721T231616_20180721T231643_022899_027BD7_C3B6 (July 21, 2018)	12	81
September 19, 2018	• S1A_IW_SLC__1SDV_20180907T231619_20180907T231646_023599_02922C_A653 (September 7, 2018) • S1A_IW_SLC__1SDV_20180919T231619_20180919T231646_023774_0297CC_519B (September 19, 2018)	12	44

Appendix D: SNAPHU Methodology

The SNAPHU tool was used to unwrap phase data and covert it to a format usable by the SNAP suite. While SNAPHU is compatible with SNAP, the tool itself was separate from the SNAP suite and required a Linux-based operating system to be run. The system that was used for performing the SNAPHU phase unwrapping contained an i7-6700k processor, 16GB DDR4 RAM, Nvidia GTX 1080TI graphics card and was using the Kubuntu 20.04 64-bit operating system. SNAPHU configuration files were generated using the SNAP Snaphu Export tool which allowed the user to input parameters such as number of rows and columns for the tile of values being calculated, tile overlap and the statistical-cost mode method that SNAPHU will use for the calculations. A tile size of 10 by 10 was used as well as an overlap of 200 pixels which was the recommended default. The TOPO (topographic) statistical-cost mode was used since the data being unwrapped was topographic. Due to the data size of the interferograms, a subset of the data was taken to reduce the computation time as well as limit the system resource usage to prevent the processes from crashing. Once configuration files and subsets were created for every interferogram, a BASH script was run to execute the SNAPHU tool on each subset to create the six unwrapped interferogram rasters.

Appendix E: Comparison of Unadjusted RPAS and Sentinel LAI Residual Values

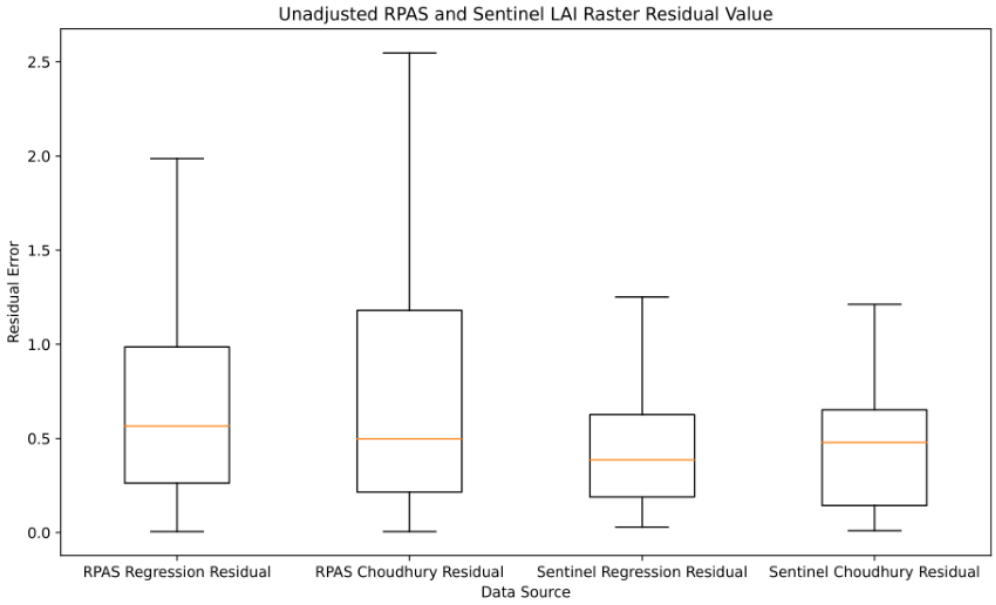

Figure E: Comparison of unadjusted RPAS and Sentinel LAI residual values.

Appendix F: Graph of CSM Yield Values

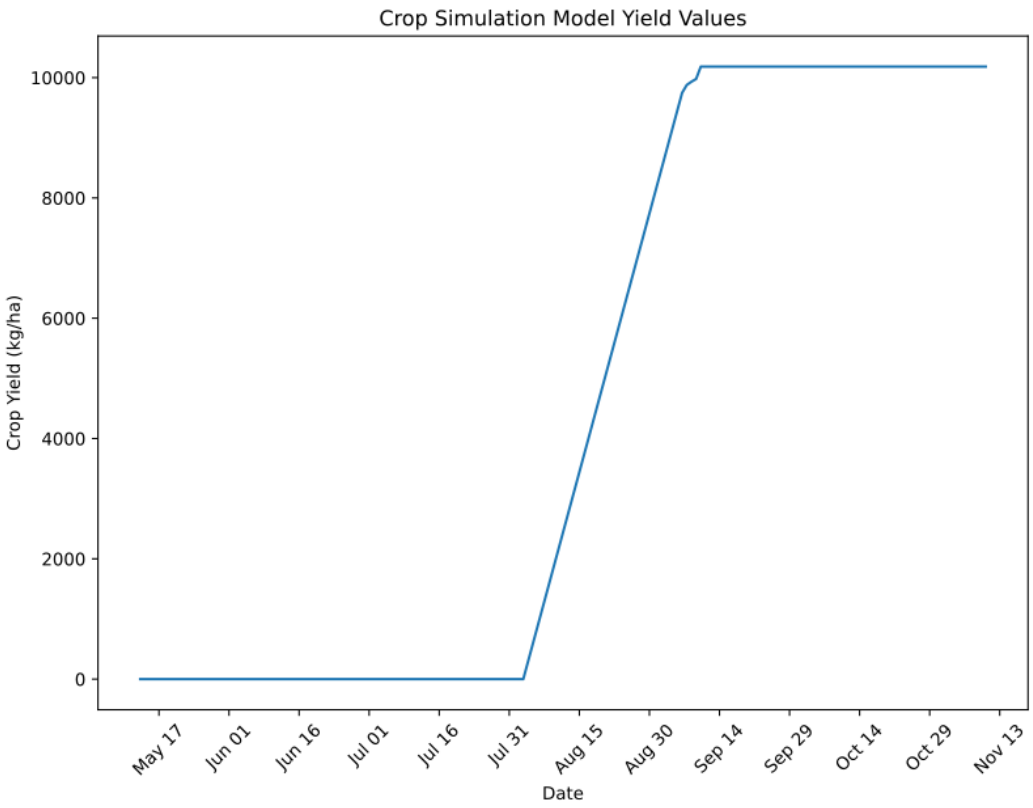

Figure F: Simulated crop yield values generated by DSSAT-CERES-Maize model.